

# Multi-Step Dst Development and Ring Current Composition Changes during the 4–6 June 1991 Magnetic Storm

30 December 2001

Prepared by

J. U. KOZYRA, M. W. LIEMOHN,  
C. R. CLAUER, and J. RIDLEY  
Space Physics Research Laboratory  
University of Michigan, Ann Arbor

M. F. THOMSEN and J. E. BOROVSKY  
Space and Atmospheric Science Division  
Los Alamos National Laboratory, NM

J. L. ROEDER  
Space Science Applications Laboratory  
The Aerospace Corporation, Los Angeles, CA

W. D. GONZALEZ  
Instituto de Pesquisas Espaciais, São Paulo, Brazil

Prepared for

SPACE AND MISSILE SYSTEMS CENTER  
AIR FORCE SPACE COMMAND  
2430 E. El Segundo Boulevard  
Los Angeles Air Force Base, CA 90245

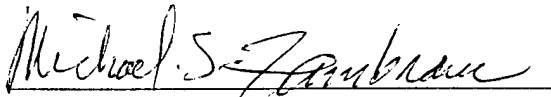
Engineering and Technology Group

APPROVED FOR PUBLIC RELEASE;  
DISTRIBUTION UNLIMITED

This report was submitted by The Aerospace Corporation, El Segundo, CA 90245-4691, under Contract No. F04701-00-C-0009 with the Space and Missile Systems Center, 2430 E. El Segundo Blvd., Los Angeles Air Force Base, CA 90245. It was reviewed and approved for The Aerospace Corporation by J. A. Hackwell, Principal Director, Space Science Applications Laboratory. Michael Zambrana was the project officer for the Mission-Oriented Investigation and Experimentation (MOIE) program.

This report has been reviewed by the Public Affairs Office (PAS) and is releasable to the National Technical Information Service (NTIS). At NTIS, it will be available to the general public, including foreign nationals.

This technical report has been reviewed and is approved for publication. Publication of this report does not constitute Air Force approval of the report's findings or conclusions. It is published only for the exchange and stimulation of ideas.

A handwritten signature in cursive script that reads "Michael S. Zambrana". The signature is written in black ink and is positioned above a horizontal line.

Michael Zambrana  
SMC/AXE

# REPORT DOCUMENTATION PAGE

Form Approved  
OMB No. 0704-0188

Public reporting burden for this collection of information is estimated to average 1 hour per response, including the time for reviewing instructions, searching existing data sources, gathering and maintaining the data needed, and completing and reviewing this collection of information. Send comments regarding this burden estimate or any other aspect of this collection of information, including suggestions for reducing this burden to Department of Defense, Washington Headquarters Services, Directorate for Information Operations and Reports (0704-0188), 1215 Jefferson Davis Highway, Suite 1204, Arlington, VA 22202-4302. Respondents should be aware that notwithstanding any other provision of law, no person shall be subject to any penalty for failing to comply with a collection of information if it does not display a currently valid OMB control number. PLEASE DO NOT RETURN YOUR FORM TO THE ABOVE ADDRESS.

1. REPORT DATE (DD-MM-YYYY) 30-12-2001		2. REPORT TYPE		3. DATES COVERED (From - To)	
4. TITLE AND SUBTITLE  Multi-Step Dst Development and Ring Current Composition Changes during the 4-6 June 1991 Magnetic Storm				5a. CONTRACT NUMBER F04701-00-C-0009	
				5b. GRANT NUMBER	
				5c. PROGRAM ELEMENT NUMBER	
6. AUTHOR(S)  J. U. Kozyra, M. W. Liemohn, C. R. Clauer, J. Ridley, M. F. Thomsen, J. E. Borovsky, J. L. Roeder, and W. D. Gonzalez				5d. PROJECT NUMBER	
				5e. TASK NUMBER	
				5f. WORK UNIT NUMBER	
7. PERFORMING ORGANIZATION NAME(S) AND ADDRESS(ES)  The Aerospace Corporation Laboratory Operations El Segundo, CA 90245-4691				8. PERFORMING ORGANIZATION REPORT NUMBER  TR-2001(8570)-4	
9. SPONSORING / MONITORING AGENCY NAME(S) AND ADDRESS(ES) Space and Missile Systems Center Air Force Space Command 2430 E. El Segundo Blvd. Los Angeles Air Force Base, CA 90245				10. SPONSOR/MONITOR'S ACRONYM(S) SMC	
				11. SPONSOR/MONITOR'S REPORT NUMBER(S) SMC-TR-02-22	
12. DISTRIBUTION/AVAILABILITY STATEMENT  Approved for public release; distribution unlimited.					
13. SUPPLEMENTARY NOTES					
14. ABSTRACT The 4-6 June 1991 magnetic storm during solar maximum conditions is analyzed to investigate two observed features of magnetic storms: (1) ring current composition changes strongly correlated with Dst changes; and (2) multi-step ring current development. A kinetic ring current drift-loss model, driven by dynamic fluxes at the nightside outer boundary, simulated this storm interval. The majority of ions in the partial ring current pass through the inner magnetosphere on open drift paths before exiting the dayside magnetopause. Losses at the magnetopause account for the fast decay during the early recovery of the storm. It is demonstrated that density and composition changes of the inner plasma sheet are transmitted along open drift paths directly into the inner magnetosphere. When ring current drift paths are open to the magnetotail (main and early recovery phases), changes in the plasma sheet drive changes in the ring current characteristics. This accounts for the ring current composition changes correlated with Dst. It is found that the early intensifications are swept out of the magnetosphere by enhanced convection and do not precondition the system. Higher plasma sheet densities and enhanced convection produced intensifications associated with later Dst minima.					
15. SUBJECT TERMS  Ring current, Magnetic storm, Solar maximum					
16. SECURITY CLASSIFICATION OF:			17. LIMITATION OF ABSTRACT	18. NUMBER OF PAGES	19a. NAME OF RESPONSIBLE PERSON
a. REPORT	b. ABSTRACT	c. THIS PAGE			James Roeder
UNCLASSIFIED	UNCLASSIFIED	UNCLASSIFIED		58	19b. TELEPHONE NUMBER (include area code) (310)336-7081

## Contents

1. Introduction.....	1
2. Observations .....	7
2.1 Solar Wind .....	7
2.2 Magnetic Activity Indices .....	9
2.3 Geosynchronous Plasma Observations .....	10
2.4 CRRES Plasma and Field Observations .....	15
3. Ring Current Model.....	18
4. Ring Current Energy Input.....	19
4.1 The Electric Field Model.....	20
4.2 Nightside Plasma Sheet Source Population .....	24
4.3 Energy Input Function .....	26
5. Simulated Ring Current: Detailed View.....	28
5.1 Ring Current Characteristics .....	28
5.2 Comparison with Satellite Observations.....	31
6. Simulated Ring Current: Globally Integrated View.....	33
6.1 Multi-Stage Dst* Development.....	33
6.2 Two-Phase Decay .....	37
6.3 Correlation between Composition Changes and Dst.....	42
7. Summary and Conclusions.....	46
References.....	50

## Figures

1. Summary of solar wind conditions and magnetic activity indices during the 4–6 June 1991 magnetic storm.....	8
--	---

2.	CRRES MICS observations of the ring current for the orbits during the June 1991 storm .....	16
3.	Plot of (a) the cross polar cap potential drop calculated from the AMIE technique, (b) the midnight auroral boundary index (MBI), (c) nightside MPA densities, (d) convection electric field at geosynchronous orbit at local midnight, (e) energy input functions to the simulation (see text) and from the <i>Burton et al. F(E)</i> relation, and (f) observed and modeled Dst*, along with the Dst* prediction from the Burton formula .....	23
4.	Plot of (a) pressure-corrected Dst, (b) nightside plasma sheet density, (c) nightside plasma sheet $T_{\perp}$ and (d) nightside plasma sheet $T_{\perp}/T_{\parallel}$ .....	25
5.	Energy densities observed by CRRES MICS and simulation results for the same times and locations for 3 outbound passes of the spacecraft.....	32
6.	Modeled Dst* from simulations, including all of the injection intervals (solid line), only the second and third injections (dotted line), and only the third injection (dashed line).....	35
7.	(a) Dst* from observations, from the model results, and from each of the species ( $H^+$ and $O^+$ ) individually. (b) $O^+$ contribution to ring current energy density in the $L = 3-5$ belt calculated from the model results (solid line, $E > 40$ keV; dotted line, all energies) and estimated from the CRRES measurements from <i>Roeder et al.</i> [1996b] and <i>Daglis</i> [1997] (symbols and crosses, respectively). (d) Total energy input rates from the simulation results from inflow through the boundary and net adiabatic drift effects. (e) Total energy loss rates from the simulation results from outflow through the boundary and charge exchange. (f) The ratio of the outflow loss rate to the charge exchange loss rate (the two quantities in the panel above), with a dashed line at unity for reference. (g) The subsolar magnetopause location (standoff distance) as computed by the <i>Shue et al.</i> [1998] formula .....	39

## Plates

1.	Twelve-hour color energy spectrogram of the magnetospheric plasma analyzer (MPA) ion and electron plasma data from 1989-095 (panels a and b) and 1989-046 (panels c and d) for June 4, 1991 .....	12
2.	The magnetospheric plasma analyzer (MPA) plasma data from 1989-095 for June 5, 1991 .....	14
3.	Dial plots of ring current pressure (energy density) in the equatorial plane, perpendicular current density in the equatorial plane, and parallel current density into the northern hemisphere ionosphere (120 km altitude).....	29

4. Dial plots of  $O^+$  percentage of number density showing oxygen-rich plasma sweeping through the system during the main phase development and oxygen-poor plasma replacing it as the activity level declines during the recovery phase ..... 44

## 1. Introduction

It is generally accepted that the ring current is formed partially from ions with direct convective access to low L values and partially from higher energy ions on closed drift paths diffusing in under the influence of fluctuating magnetic fields [Lyons and Williams, 1984; Lyons and Schulz, 1989]. Chen *et al.* [1994] showed that the energy demarcating these two populations at L=3 is ~160 keV. Since ions in the energy range 10 – 200 keV are responsible for the majority of the ring current energy content (and thus Dst\* variation), most of the ring current forms through convective transport. The high-energy tail of the ring current can be built up significantly through diffusive transport if the main phase is longer than ~6 hours. In order for particles with direct convective access to become part of the ring current, they must have drift times that are less than half of the storm main phase. These ions remain on the nightside convecting inward until the convection electric field weakens at the end of the main phase trapping them on closed drift paths. Lyons and Schulz [1989] site 3 hours as a typical length for the main phase of a major magnetic storm. This is consistent with the threshold value of 3 hours (2 hours) duration of southward IMF < -10 nT (< -5 nT) found to lead to major (moderate) magnetic storms with 80% occurrence probability (see review by Gonzalez *et al.* [1994]). The key points in this view are that the ring current evolution is largely separate from the plasma sheet dynamics after the minimum in Dst\*, and throughout the storm the dominant losses are through interactions of energetic ions with thermal populations and waves. During the recovery phase of the magnetic storm, the ring current is symmetric, nondivergent, and decaying through collisions with the background geocorona and plasmasphere [see recent review by Daglis *et al.*, 1999].

This picture is undoubtedly true for some magnetic storms. However, magnetic clouds (a key solar wind driver of major magnetic storms) can have time scales for southward IMF as long as 12 hours and a slow smooth rotation of southward to northward IMF as the cloud moves past the Earth (see examples in Gonzalez *et al.*, [1999] and in Liemohn *et al.* [2001a]). The response

of the magnetosphere is dramatic. Plasma sheet ions, moving on open drift paths into the inner magnetosphere, are not captured on closed drift paths but move through to the dayside magnetopause and are lost. In fact “flow-out” losses at the dayside magnetopause dominate other losses throughout the main and most of the early recovery phase of the storm [Takahashi *et al.*, 1990; Ebihara and Ejiri, 1998; Liemohn *et al.*, 1999]. Even storms with a minor  $O^+$  component can exhibit a 2-phase decay [Liemohn *et al.*, 1999, 2001]. In a storm with a large ring current  $O^+$  component (like the 4 June 1991 storm studied here), charge exchange can make a significant contribution at times. The ring current is highly asymmetric [Kozyra *et al.*, 1998a; Ebihara and Ejiri, 1998; Liemohn *et al.*, 1999, 2001a, b] with up to 90% of the energy flowing along open drift paths in the main phase, making it an intense long-duration partial ring current. The divergence of this intense partial ring current creates field-aligned currents, which close through the subauroral ionosphere mostly poleward into the region I currents but also a small amount closes azimuthally through the westward electrojet [cf. Crooker and Siscoe, 1974]. This produces long-duration and intense subauroral electric fields.

A step function decrease in the southward IMF instantaneously traps all ring current particles in the inner magnetosphere on closed drift paths. The ring current then decays slowly through collisional losses. In this case, there is no distinctive two-phase decay but a single phase with a slowly increasing decay time-scale as species with short charge exchange collision lifetimes are preferentially removed. However, a long slow rotation of interplanetary magnetic fields from south to north in the cloud gradually converts open to closed drift paths, giving ions time to drift to the dayside magnetopause and be lost before their drift paths can become closed. At the same time, the plasma sheet ion distribution is changing.

To more clearly illustrate the effects on the ring current decay time-scale of each of these elements, consider first a slow decrease in the convection electric field with a fixed plasma sheet density. As the convection field decreases, new plasma, moving in on the nightside to replace ions being lost at the dayside magnetopause, travels along open drift paths that penetrate less deeply into the inner magnetosphere with weaker adiabatic energization than the plasma drifting

out the dayside magnetopause. A net energy loss occurs. The amount and time-scale for the energy loss, and the strength of the ring current that eventually becomes trapped in the late recovery phase, depends on the time scale for the electric field decrease.

Now consider a decrease in the plasma sheet density with a fixed convection strength. The higher density plasma, moving out of the dayside magnetopause on open drift paths, is gradually replaced by lower density plasma moving through the nightside boundary. To completely replace the higher density with lower density plasma, and come to a new lower Dst\* value, takes a time-scale on the order of the average drift time from the nightside plasma sheet to the dayside magnetopause (as low as 4-6 hours). *Ebihara and Ejiri [2000]* have demonstrated that ring current recovery can also be produced solely by plasma sheet temperature changes.

The actual fast “flow-out” time-scale is a combination of time-scales associated with the electric field decline and those associated with plasma sheet density and temperature changes. The conversion from the fast “flow out” losses associated with open drift paths to the slower “charge-exchange” losses associated with closed drift paths is responsible for the two-phase decay.

Because the partial ring current is connected via open drift-paths to the inner plasma sheet, the dynamical changes in the plasma sheet in response to solar wind forcing directly drive the ring current throughout the main and early recovery phase of magnetic storms with 2-phase decay. For example, the passage of a superdense plasma sheet region through the inner magnetosphere during the November 1993 magnetic storm produced a factor of 3 increase in the strength of the developing ring current [*Kozyra et al., 1998c*]. Similarly, the ring current buildup resulting from convection alone could not account for the entire decrease in Dst during the October 1995 magnetic cloud event [*Jordanova et al., 1998*]. For storms with two-phase decay, by the time the ring current becomes symmetric in the late recovery phase, and the plasma sheet dynamics decouple from the ring current dynamics, most of the energy of the ring current has already been dissipated. The present study presents further examples of the far-reaching consequences of the main and early recovery phase partial ring current configuration by

demonstrating its role in the apparent mass-dependence of early-recovery-phase loss processes [c.f., *Daglis*, 1997] and in multi-stage Dst development [*Kamide et al.*, 1998].

In general the variation with time of the percent O<sup>+</sup> content looks like the mirror-image of the Dst\* variation [*Daglis*, 1997]. Similar behavior has been reported for a variety of storms observed by AMPTE/CCE [*Gloeckler and Hamilton.*, 1987] and CRRES [*Roeder et al.*, 1996a, b; *Daglis*, 1997]. During the ring current build-up, this is understood to be driven by changes in the O<sup>+</sup> content of the ring current source populations with magnetic activity. However, in the early recovery phase, the preferential removal of O<sup>+</sup> from the ring current and the fast decay time scales led *Hamilton et al* [1988] to propose O<sup>+</sup> charge exchange as the underlying mechanism for the early recovery and, in fact, to propose the difference in charge-exchange lifetimes between O<sup>+</sup> and H<sup>+</sup> to account for the two-phase decay typical of major magnetic storms. Oxygen charge-exchange lifetimes are relatively short (~7-10 hrs at L~3), whereas hydrogen collisional lifetimes become very long (1 day to tens of days) at energies between 50 keV and 200 keV [c.f., *Fok et al.*, 1991]. After most of the oxygen is removed, decay time-scales are controlled by the hydrogen component of the ring current and become decidedly longer. However, ring current simulations were unable to reproduce either the fast time scales of the early recovery phase loss or the two phase decay [*Kozyra et al.*, 1998b], despite the fact that the model was based on the *Hamilton et al.* [1988] AMPTE/CCE observations.

This study will demonstrate that the dramatic composition changes that occur in the ring current during the early recovery phase of the 4-6 June 1991 storm, are produced by a combination of changes in composition of the ring current source population in the plasma sheet and mass-dependent loss processes as was suggested [c.f., *Hamilton et al.*, 1988; *Daglis et al.*, 1999]. During the decrease in magnetic activity following the main phase, increasingly oxygen-poor plasma sheet source populations sweep through the inner magnetosphere on open drift paths which are gradually being converted to closed drift paths. At the same time, the more oxygen-rich populations, associated with the main phase plasma sheet source, are being lost at the dayside magnetopause. This transition from relatively oxygen-rich to oxygen-poor plasma occurs

throughout the early recovery phase. During this storm, as opposed to other simpler two-phase storms, the early recovery phase begins with an abrupt northward turning of the IMF which traps the ring current on closed drift paths and produces an interval within which charge exchange temporarily dominates the loss. Following this interval the recovery phase exhibits the characteristics of a two-phase decay wherein the transition between open and closed drift trajectories marks the transition between fast and slow recovery phases.

The relationship between the ring current and plasma sheet dynamics introduces the interesting possibility that preconditioning of the plasma sheet can significantly alter the response of the inner magnetosphere to solar wind forcing during a magnetic storm. Superposed epoch analyses of magnetic storms indicate that multi-stage intensifications are more effective than single-stage intensifications at producing large magnetic storms [*Kamide et al.*, 1998]. This is inferred from the fact that the percentage of two-stage storms increases with storm size. In general, two-stage storms result from successive impacts of different regions of southward IMF on the magnetosphere. The first impact triggers a magnetic storm, which does not have time to recover, before the second impact begins. The second decrease in the Dst index is usually deeper than the first although the magnitude of the second interval of southward IMF is, in general, not significantly different from the first interval. An important question is whether the first hit preconditions the inner magnetosphere with a pre-existing ring current population that is further amplified by the second impact. *Chen et al.* [2000] demonstrated that two intervals of enhanced convection are not inherently more effective at producing a strong ring current than one longer interval (adjusted so that the two different main phases produce similar diffusion coefficients). *Chen et al.* [1994] point out that another important factor in determining the strength of the ring current is the length of the main phase. Longer main phases produce stronger ring currents in general because they allow more time for the high energy tail of the ring current to build up as ions without convective access to the inner magnetosphere diffuse inward. A study of two-stage storms by *Kamide et al.* [1998] indicates that, statistically, two-stage storms have longer main phases than single-stage ones. Finally, *Kozyra et al.* [1998a] demonstrated that the plasma sheet

density can change markedly between the two intervals of enhanced convection responsible for the storm development. The role of plasma sheet density variations in producing the most intense double-dip Dst magnetic storms needs to be clarified.

The multi-stage development of the 4-6 June 1991 magnetic storm is a more general example of the two-stage storm development studied by *Kamide et al.* [1998]. This study will show that the enhanced convection associated with an interval of southward Bz clears out the majority of pre-existing ring current particles and replaces them with new populations from the near-Earth plasma sheet. Variations in plasma sheet density in combination with changes in the convection strength determine the relative magnitudes of the ring current intensifications during the storm. Because of the open drift path geometry of the main phase ring current and the similar or increasing IMF Bz in each subsequent injection, earlier injections are swept out of the dayside magnetopause as new material moves into the inner magnetosphere in response to increasing magnetic activity. The inner magnetosphere retains little or no memory of these previous injections. It is suggested that preconditioning occurs in a multi-step magnetic storm development through the cumulative effects of the sequence of solar wind drivers on the plasma populations that form the near-Earth plasma sheet [c.f., *Kozyra et al.*, 1998a].

As discussed above, *Liemohn et al.* [1999, 2001a] showed that dayside loss due to convective drift to the magnetopause is the largest loss process during the early recovery phase of the storms they examined. This is not contradictory to previous observational and modeling studies, since *Liemohn et al.* [1999] used essentially the same model as the one developed by *Jordanova et al.* [1997, 1998]. While dayside losses were included in the simulation of ring current development during the October 1995 magnetic storm by *Jordanova et al.* [1998], the study focused mainly on the relative effect of various collisional mechanisms on ring current decay. It was thus found that charge exchange was the most important loss mechanism of the collisional losses they considered. It was as well demonstrated that about 10% changes in Dst magnitude occurred due to difference in convective transport and losses through the dayside boundary caused by a rotation of the symmetry line of the Volland-Stern convection model.

To address the issues outlined above, the paper is organized as follows. Details of solar wind and magnetospheric observations during the 4-6 June 1991 storm are presented in Section 2. The ring current simulation model is described in Section 3. Energy influx through the nightside outer boundary of the ring current model is simulated throughout the storm using a model of the convection electric field and measured source populations at geosynchronous orbit are presented in Section 4. The techniques for producing these energy inflows are also described in Section 4, along with comparisons to energy input functions using upstream solar wind parameters. Detailed simulation results are presented and compared to observations in Section 5. Section 6 explores the globally-averaged behavior of the ring current, specifically investigating the physical mechanisms behind the ring current development and decay and the associated composition changes. Section 7 summarizes the study and lists the conclusions.

## **2. Observations**

### **2.1 Solar Wind**

The solar wind plasma values (Figures 1a - 1c) all show a dramatic increase around 1530 UT on June 4 with the density and speed reaching peak values at 0000 UT on June 5. At 1800 UT on June 5 another interval of enhanced solar wind density and velocity encounters the magnetosphere with solar wind density reaching  $47 \text{ cm}^{-3}$  and velocity rising back up to 600 km/s. Significant data gaps exist in the IMP 8 data on June 4 from 0954-1255 UT, on June 5 from 0556-1010 UT and from 1736-2047 UT. Unfortunately, these later two data gaps occurred during the two strongest ring current intensifications, shown as deep minima in the Dst index (Figure 1g). Another solar wind data gap exists early on June 6, but by this time the storm is already decaying. The IMF  $B_z$  (Figure 1d) component shows dramatic swings between -30 nT and +20 nT throughout the storm, but is mostly southward during the main phase of the event.

The motional electric field of the solar wind,  $E_y$ , defined as the cross product of the flow vector with IMF  $B_z$  is shown in Figure 1e.  $E_y$  has been closely related to the cross-tail electric

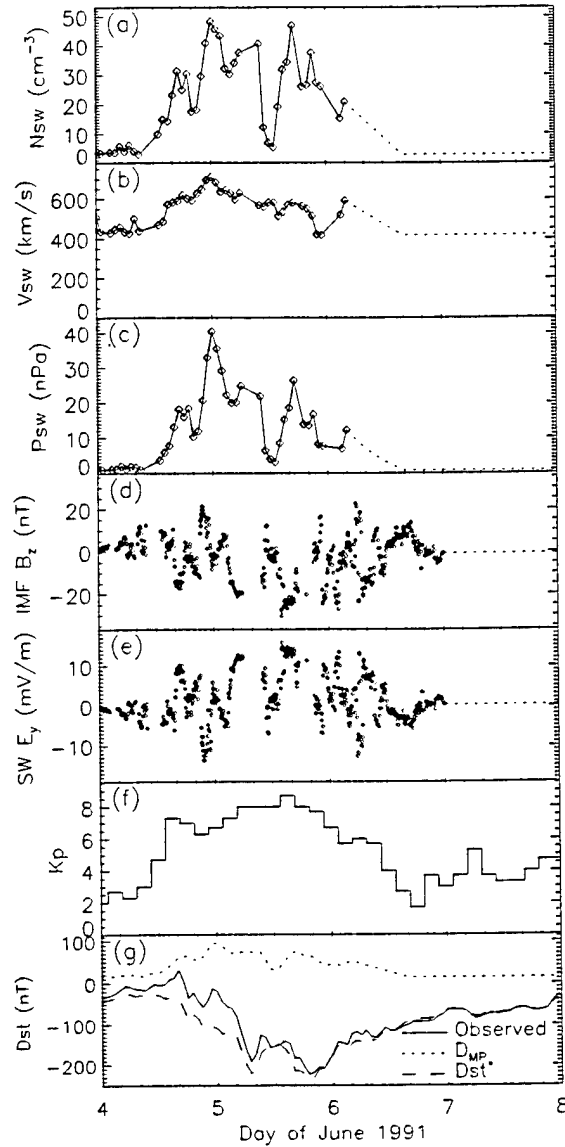


Figure 1. Summary of solar wind conditions and magnetic activity indices during the 4–6 June 1991 magnetic storm. Displayed are (a) solar wind density, (b) solar wind velocity, (c) solar wind dynamic pressure, (d) IMF  $B_z$ , (e) solar wind  $E_y$ , (f)  $K_p$ , and (g) observed Dst, including the contribution of magnetopause currents to Dst and the derived pressure-corrected Dst ( $Dst^*$ ). The dotted line extending past the end of the solar wind data is the extrapolation used in the simulations.

field in the magnetosphere [Gonzalez *et al.*, 1989; Tsurutani *et al.*, 1992], and has been shown to control the convection of plasma from the magnetotail through the inner magnetosphere. During most of the main phase of the storm,  $E_y$  is large and positive, although this quantity varies considerably throughout the storm. Three intervals of strong  $E_y$  are associated with the 3 intensifications of the ring current over the course of the storm. In addition, the 3 maxima of  $E_y$  are successively larger.

## 2.2 Magnetic Activity Indices

Also shown in Figure 1 are the planetary indices of Kp and Dst from ground-based magnetometer observations [cf., *Mayaud*, 1980]. Kp (Figure 1f) rapidly ramps up midway through June 4 from 2 to 7+, and remains greater than 6 until early on June 6. The Dst index (Figure 1g) shows a storm sudden commencement (SSC) near 1400 UT on June 4. This is followed by three ring current intensifications producing minima in the Dst index of magnitude -50 nT at 2200 UT on June 4, -190 nT at 0800 UT on June 5, and -219 nT at 2000 UT later that day. These minima in the Dst (maxima in ring current energy) are all associated with southward turnings of the IMF with minimum Bz values near -15 nT, -20 nT, and -25 nT, respectively (Figure 1d). The storm shows a classic two-phase decay, with ~130 nT recovery occurring over the first 15 hours (after the final Dst minimum) followed by a slow decline in intensity (~35 nT/day) over the next several days. In the Dst panel, two other values are also shown. The first is the contribution to Dst from the magnetopause Chapman-Ferraro currents, calculated from the observed solar wind parameters according to

$$D_{mp} [nT] = 0.02 v_{sw} [km/s] \sqrt{n_{sw} [cm^{-3}]} \quad (1)$$

from *Burton et al.* [1975]. This is always a positive value because of the eastward flow of this current. The SSC is a direct consequence of the initial pressure pulse, and it also explains the Dst oscillation near 0000 UT on June 5. Near 1200 UT on June 5, a brief Dst recovery is produced by a northward turning of the IMF Bz. This recovery occurs despite a simultaneous decrease in the solar wind dynamic pressure which should produce a decrease in Dst as the

positive contribution from the magnetopause current lessens. Also shown in this panel is  $Dst^*$  (the assumed ring current contribution to the Dst index), which is obtained by correcting the observed Dst index for the effects of the diamagnetic Earth and removing the contribution from the magnetopause currents.  $Dst^*$  is given by:

$$Dst^* = \frac{Dst}{1.3} - D_{mp} \quad (2)$$

where the divisor of Dst is a coefficient to account for the diamagnetic effect of the Earth [Dessler and Parker, 1959; Langel and Estes, 1985]. This quantity is directly comparable to estimates of Dst from the ring current strength, such as the Dessler-Parker-Sckopke (DPS) relation [Dessler and Parker, 1959; Sckopke, 1966],

$$Dst^* [nT] = \frac{E_{RC} [keV]}{2.51 \times 10^{29}} \quad (3)$$

which equates  $Dst^*$  to the total kinetic energy in the ring current,  $E_{RC}$ . The DPS relation was derived from the Biot-Savart law by integrating the currents generated from particle gyration and magnetic gradient-curvature drifts in the inner magnetosphere, and is valid for any particle phase-space distribution [cf. Sckopke, 1966; Carovillano and Siscoe, 1973]. This calculation for  $Dst^*$  will be used in the analysis of the simulation results presented below. Note that a dipole magnetic field was assumed in obtaining the denominator coefficient in (3). After correcting for the rather large contributions of the magnetopause currents to the Dst index, the two deep minima in  $Dst^*$  are comparable in intensity (the third is still slightly deeper, as will be discussed later).

### 2.3 Geosynchronous Plasma Observations

The Los Alamos National Laboratory (LANL) maintains several geosynchronous spacecraft with onboard plasma spectrometers measuring particle distributions relevant to the ring current. This data set consists of observations from the magnetospheric plasma analyzer (MPA) which measures the distributions of ions and electrons up 50 keV [McComas *et al.*, 1993], and the synchronous orbit particle analyzer (SOPA) which measures the distributions of

ions and electrons above 50 keV [*Belian et al.*, 1992]. Because the energy range of MPA captures the bulk of the near-Earth plasma sheet that feeds the ring current, data from this instrument will be shown here in detail.

There were two LANL geosynchronous satellites with MPA instruments making observations during the June 1991 storm. Satellite 1989-046 was located at 195° E longitude and satellite 1990-095 was sampling at 97.5° E longitude. These satellites observed the response of the magnetosphere (at the outer boundary of the ring current simulation volume) to changing solar wind inputs. On the nightside, this region contains information on the ring current source populations and the strength of the driving convection electric fields and thus is of primary interest to this study.

The geosynchronous observations give an interesting overview of activity conditions from just-prior to the storm through its recovery. Plate 1 is a 24-hour color energy spectrogram for ions and electrons which survey conditions on June 4 from both geosynchronous satellites. In the latter half of the day during the 1st ring current intensification, 1989-046 was on the dawn side and 1990-095 was in the dusk sector. Activity levels were already elevated prior to the storm with a baseline value of Dst\* near -50 nT and a Kp ~ 2-3. The MPA observations confirm these elevated activity levels through observations of the thermal plasma structures. Satellite 1989-046 sees no evidence of the plasmasphere in low energy ion observations on the duskside early in the day, even though it is commonly observed there during times of low magnetic activity [*Elphic et al.*, 1996]. The absence of the plasmasphere indicates that it was eroded by previous activity and never allowed to refill prior to the onset of the June 1991 storm. The absence of the electron plasma sheet across the nightside indicates a very weak convection.

At 1600 UT, the electron plasma sheet overtakes 1989-046 near dawn (0630 hrs MLT) indicating the abrupt onset of enhanced activity. Prior to this time the spacecraft had been moving from midnight toward the dawn side without observing any indication of the active plasma sheet. At this same time, 1989-046 begins to observe ions in its highest energy channels. At ~2200 UT, 1989-046 observes a plasmaspheric ion drainage plume on the dayside in its

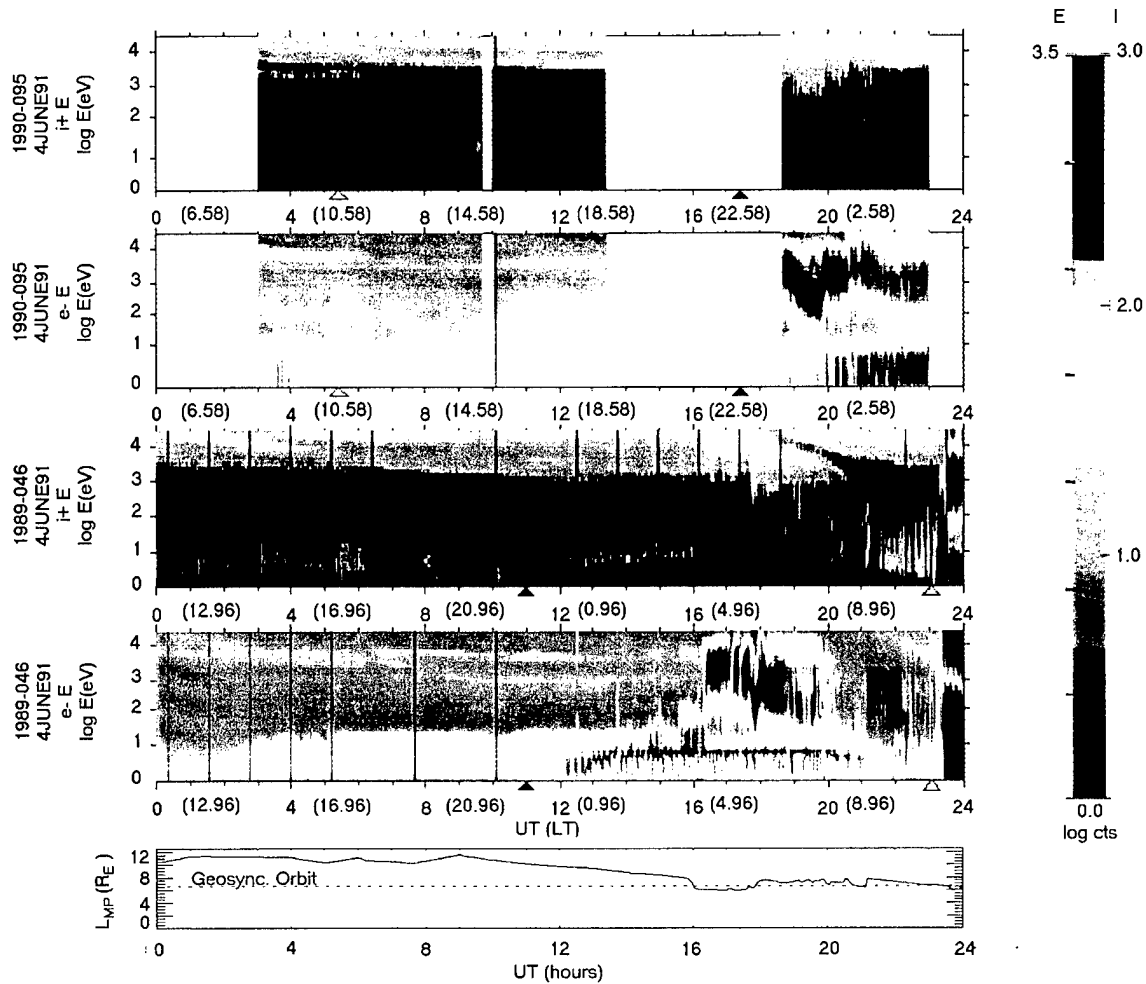


Plate 1. Twelve-hour color energy spectrogram of the magnetospheric plasma analyzer (MPA) ion and electron plasma data from 1989-095 (panels a and b) and 1989-046 (panels c and d) for June 4, 1991. Open (filled) triangles on the UT axis indicate local noon (midnight). The lower panel shows the subsolar magnetopause standoff distance as predicted by the *Shue et al.* [1998] model (solid line), as well as geosynchronous orbit (dotted line).

lowest energy channels in the pre-noon sector. This indicates that the plasmasphere is being eroded by the increased magnetic activity. Finally at 2330 UT, 1989-046 observes the magnetosheath near local noon as the magnetosphere is compressed inside geosynchronous orbit by a  $> 40$  nPa spike in the solar wind dynamic pressure accompanied by southward IMF. The bottom panel of Plate 1 shows the *Shue et al.* [1998] prediction of the magnetopause standoff distance, including when the magnetopause was inside of geosynchronous orbit. There is excellent agreement between the Shue et al model prediction and the observed encounter with the magnetosheath.

Plate 2 (MPA measurements from both satellites on June 5) paints a picture of a highly disturbed magnetosphere. Early on June 5 (0300-0700 UT) during the large second ring current intensification, 1989-046 was in the dusk sector and later (1500-1900 UT) during the large third intensification was in the dawn sector. Satellite 1990-095 covered the dayside and duskside, respectively, during this same interval. Again, the bottom panel shows the *Shue et al.* [1998] noon magnetopause location, with several extended periods of compression of this boundary inside of geosynchronous orbit. Over the first half of the day, there is excellent agreement between these predictions and times of magnetosheath encounters by 1989-046 and 1990-095 at dayside MLTs. Later in the day, 1990-095 is in the wrong local time sector to observe the compressed magnetopause. Satellite 1989-046 briefly encounters the magnetosheath around 2140 UT (very near local noon), just prior to the time interval predicted by the Shue et al. model. This encounter is much briefer than the predictions even though the satellite remains in the post-noon sector for some time where the compression should be the most pronounced. However, at this time the ring current intensification is at its maximum with Dst values  $< -200$  nT. The inflation of the magnetic field by a strong ring current is not explicitly taken into account in the Shue et al. model prediction and may introduce significant errors. Just after reentering the magnetosphere from the magnetosheath earlier in the day (0200-0400 UT), 1989-046 encounters a plasmaspheric drainage plume in the lowest energy ion channels indicating a plasmasphere that is still eroding and reconfiguring in the presence of strong magnetospheric

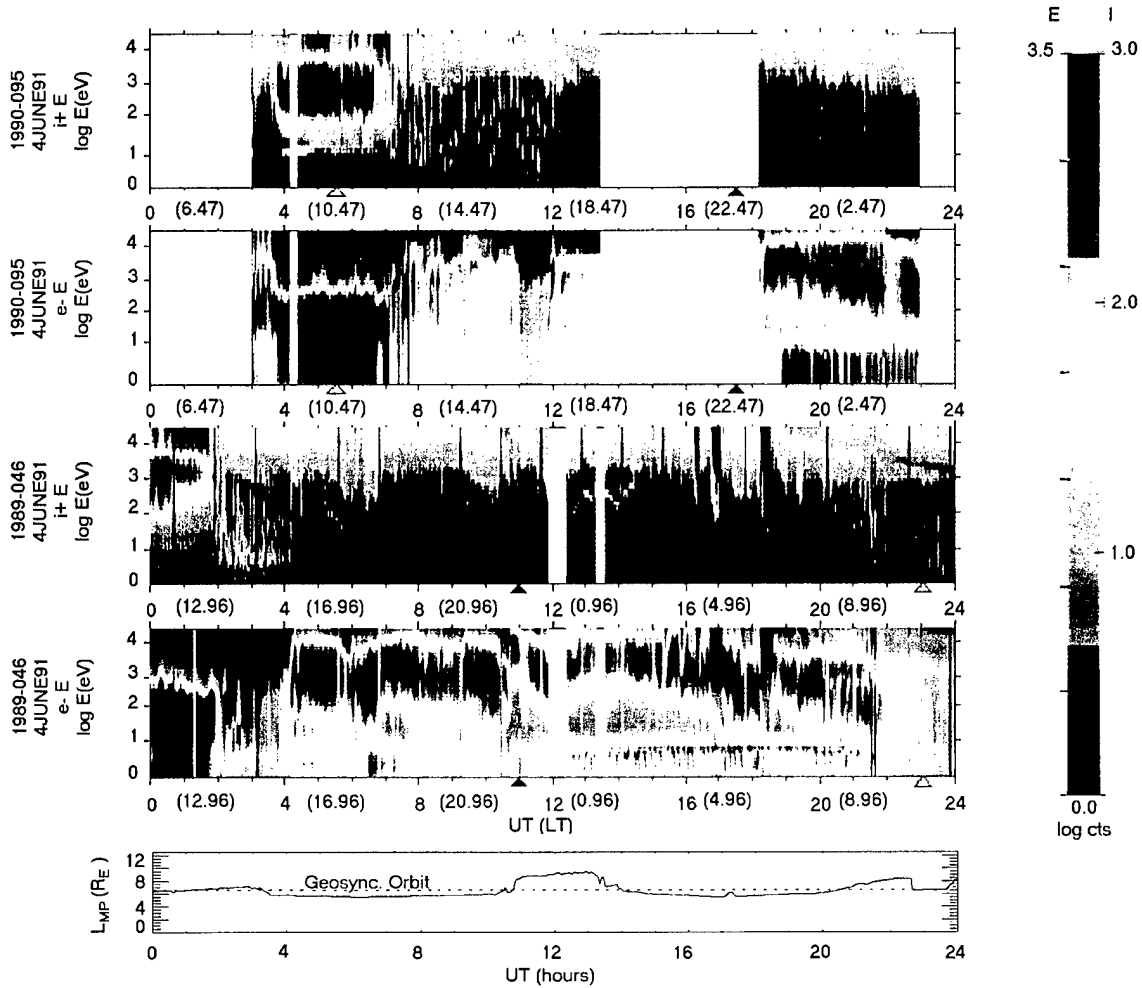


Plate 2. The magnetospheric plasma analyzer (MPA) plasma data from 1989-095 for June 5, 1991. Open (filled) triangles on the UT axis indicate local noon (midnight). The lower panel shows the subsolar magnetopause standoff distance as predicted by the *Shue et al.* [1998] model (solid line), as well as geosynchronous orbit (dotted line).

convection. The electron and ion plasma sheets observed by 1989-046 and 1990-095 are highly irregular with brief excursions of the satellite into the magnetotail lobes (indicated by plasma flux dropouts). These lobe encounters were previously reported by *Moldwin et al.* [1998] and indicate highly-stretched and distorted magnetic field geometries at geosynchronous orbit.

#### 2.4 CRRES Plasma and Field Observations

The Magnetospheric Ion Composition Spectrometer (MICS) instrument on the CRRES spacecraft was making observations of the ring current during the June 1991 storm. CRRES is in a geosynchronous transfer orbit with a perigee of 350 km, an apogee of 33,584 km and inclination 18.1°. The magnetic local time of the apogee of the CRRES orbit during the 4-6 June 1991 magnetic storm was 19.4 hours so the data ranges from local dusk to midnight. The MICS instrument measures the mass, energy, and charge state of particles over the energy range from ~1 keV/q to 426 keV/q [*Wilken et al.*, 1992; *Koga et al.*, 1992]. Of particular importance for this study are the composition measurements. High radiation backgrounds from the March 1991 great magnetic storm complicate the retrieval of accurate composition information. MICS observations of the June 1991 storm were reported on previously [*Roeder et al.*, 1996 a, b; *Daglis*, 1997] and will be summarized briefly here.

The ion energy densities were dominated by  $H^+$  prior to the storm and were larger than normal quiet-time populations seen by CRRES because of previous geomagnetic activity. This is in agreement with the high pre-storm  $|Dst|$  levels (see Figure 1g) and the absence of plasmaspheric observations by the LANL geosynchronous satellites prior to the storm onset (see Plate 1). Figure 2 shows a plot of ring current observations from CRRES MICS for orbits during the 4-8 June 1991. Shown here is the L shell of the spacecraft (Figure 2a), the magnetic latitude of the spacecraft (Figure 2b), the local ion energy density for  $E \geq 40$  keV (Figure 2c), only plotted when there were sufficient data points to produce a valid moment calculation, and the percent contribution to this energy density from  $H^+$  (Figure 2d). Clearly seen in each satellite pass is the spatial variation in the hot ion pressure, decreasing with increasing radial distance, as expected

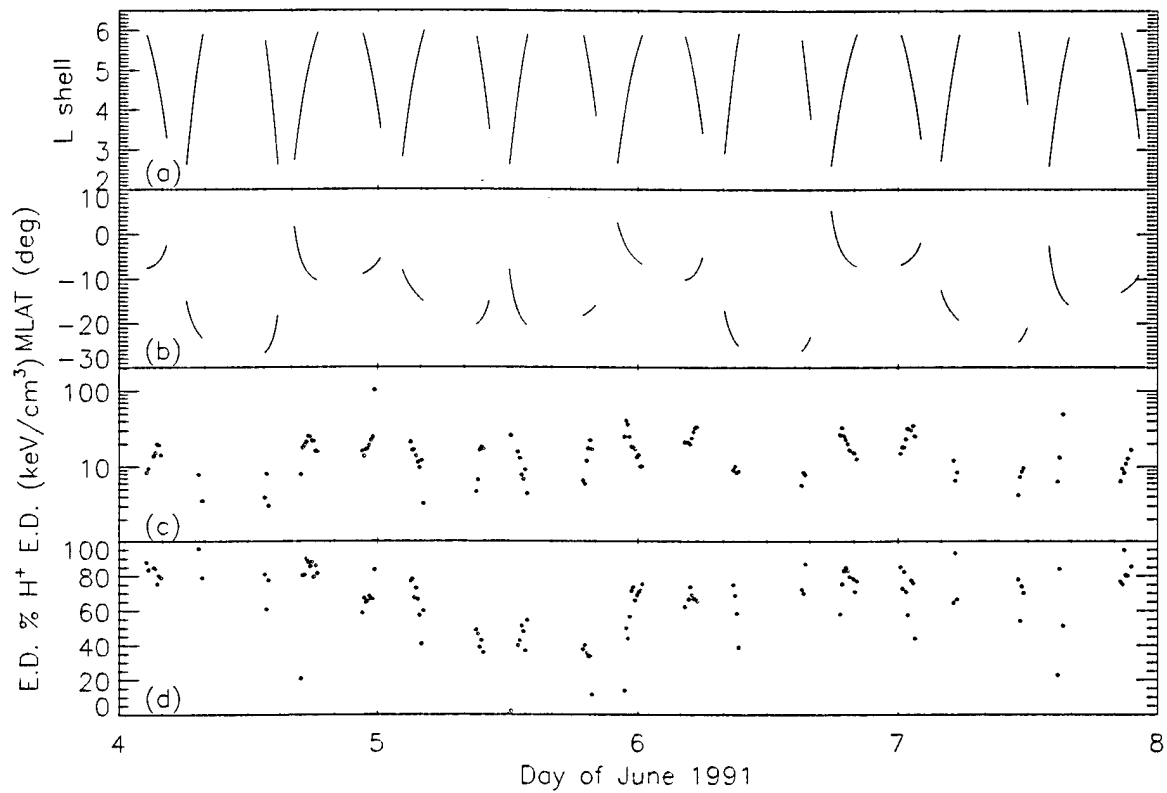


Figure 2. CRRES MICS observations of the ring current for the orbits during the June 1991 storm. Shown are (a) the satellite L-shell, (b) magnetic latitude, (c) the summed local ion energy density for  $E \geq 30$  keV, and (d) the percent  $H^+$  contribution to that value.

from adiabatic conservation. Also seen is the bulk change in composition during the storm, with  $H^+$  dominance on June 4, a significant  $O^+$  contribution on June 5, and an eventual return to  $H^+$  dominance on June 6 and 7.

*Roeder et al.* [1996b] calculated the Dst variation from the total energy measured in-situ by CRRES MICS in the ring current, extrapolated globally assuming local time symmetry and pitch-angle isotropy. The observed particle fluxes accounted for only 50-70% of the Dst variation. Similar calculations gave 30-50% for the great magnetic storm on March 23, 1991 [*Roeder et al.*, 1996a] and 24-84% for the great magnetic storm during February 1986 [*Hamilton et al.*, 1988]. Some inaccuracy in these estimates results from using a local satellite measurement to estimate a global quantity. More importantly, an instrumentally imposed lower energy cutoff in the tens of keV is often used. While such a cutoff is insignificant when measuring the quiet-time ring current, these estimates often miss the bulk of the stormtime ring current, which often has an average energy near 40 keV [e.g., *Liemohn et al.*, 2001a]. In addition, they do not take into account the ring current self-field that acts to weaken the magnetic field in the inner magnetosphere. The weakened field results in faster ion drift speeds (stronger current) for the same total ring current energy and thus a deeper Dst depression at the Earth's surface. Models indicate the self-energy is between 7% and 34% of the ring current kinetic energy for an approximately -100 nT magnetic field depression (see review by *Carovillano and Siscoe*, [1973]). Thus considering only the ring current, most of the Dst\* index can in general be reproduced. Small contributions from tail currents, the electron ring current, the substorm current wedge, and closure of the partial ring current system likely account for the remainder. As will be discussed later, the present ring current simulation produces nearly 100% of the Dst variation from the ring current energy alone and is thus an overestimate of the true energy content. This possible overestimate likely originates from inaccuracies in the time-dependent magnitude of the convection electric field model and the use of a static dipole magnetic field description.

### 3. Ring Current Model

Several theoretical computer models exist for simulating the terrestrial ring current (see review by *Wolf and Spiro* [1997]). While all are bounce-averaged kinetic drift models, each has its own distinct approach to the solution of this problem. Among the models are the particle-tracking codes of *Wodnicka* [1989, 1991], *Takahashi et al.* [1990, 1991], *Chen et al.* [1994, 1998, 1999], and *Ebihara and Ejiri* [1998], which follow weighted plasma packets through given electric and magnetic fields, assuming some loss time-scale. Another approach is to solve the kinetic equation with a Fokker-Planck collision operator, as has been done by *Fok et al.* [1993, 1995, 1996], *Jordanova et al.* [1994, 1996, 1997, 1998], *Bourdarie et al.* [1997], and *Liemohn et al.* [1999, 2001a]. These models also assume electric and magnetic fields, but are more rigorous in their inclusion of loss processes. A different technique was used by *Harel et al.* [1981], which self-consistently couples the energetic particle motion to the magnetospheric convection electric fields, yet uses a less sophisticated particle loss algorithm and distribution function [see also *Wolf et al.*, 1982; *Wolf*, 1983; *Spiro and Wolf*, 1984]. A simplified and parameterized version of this last technique has also been developed [*Weiss et al.*, 1997; *Wolf et al.*, 1997; *Lambour et al.*, 1997]. Each of these approaches has its specific advantages, being well suited to addressing some aspect of the ring current, and has been used to advance our understanding of the field.

The code to be used for this analysis is the same one used by *Liemohn et al.* [1999, 2001a], based on one originally developed by *Fok et al.* [1993] and *Jordanova et al.* [1996]. This ring current-atmosphere interaction model (RAM) solves the time-dependent, gyration- and bounce-averaged kinetic equation for the phase-space distribution function  $f(t, R, \varphi, E, \mu_0)$  of a chosen ring current species. The five independent variables are, in order, time, geocentric distance in the equatorial plane, magnetic local time, kinetic energy, and cosine of the equatorial pitch angle. The code includes collisionless drifts, energy loss and pitch angle scattering due to Coulomb collisions with the thermal plasma, charge exchange loss with the hydrogen geocorona, and precipitative loss to the upper atmosphere. See *Jordanova et al.* [1996] for a detailed

derivation of these terms. Solution of the kinetic equation is accomplished by replacing the derivatives with second-order accurate, finite volume, numerical operators. Note that this is not a particle-tracking code but actually a several-thousand-fluid calculation (the "fluids" being the grid cells in velocity-space) solved for several thousand spatial cells every time step in the simulation (typically 5 to 20 s). The source term for the distribution function is the outer simulation boundary, where observed particle fluxes from geosynchronous orbiting satellites are applied as input functions. For additional details on the present state of the model used in this study, see the discussion presented by *Liemohn et al.* [2001a].

#### 4. Ring Current Energy Input

Recent ring current simulations [*Fok et al.*, 1996; *Kozyra et al.*, 1998a, b, c; *Jordanova et al.*, 1998, 1999; *Ebahara and Ejiri*, 1998; *Liemohn et al.*, 1999, 2001a] and statistical studies [*Thomsen et al.*, 1998] indicate that the plasma sheet is the main source of particles for the ring current. The strong correlation between geosynchronous plasma sheet density and the Dst index implies that ionospheric and solar wind particles must, for the most part, be deposited in the plasma sheet downtail and then be moved Earthward and accelerated to form the injection boundary [*Mauk and McIlwain*, 1974]. Particles at the nightside injection boundary are moved Earthward through geosynchronous orbit (the outer boundary of the ring current model) under the action of enhanced stormtime convection electric fields. These particles adiabatically increase in energy and form the stormtime ring current. The manner in which the plasma sheet source characteristics are driven by solar and solar wind inputs is not yet fully understood. However, it is very clear that the changes in the plasma sheet source populations greatly impact ring current characteristics and their evolution throughout magnetic storms [c.f., *Kozyra et al.*, 1998a, c; *Liemohn et al.*, 1999].

This discussion will focus on the two main drivers of the strength of the ring current: the magnetospheric convection electric field and the near-Earth plasma sheet phase-space distribution. It is well known that during geomagnetic storms, the intensity of both of these

quantities is enhanced. Further, the relative timing of these enhancements is critical to ring current development.

#### 4.1 The Electric Field Model

*Burke et al.* [1998] examined the evolution of the convective electric fields ( $E_y$  GSE) at high and low altitudes in the dusk local time sector during the 4-6 June 1991 magnetic storm. This study utilized observations at low altitude from the ion drift meter (IDM) on the Defense Meteorological Satellite Program Flight 8 (DMSP F8) and at high altitude (near the equatorial plane) from the electric field experiment (EFI) on the Combined Release and Radiation Effects Satellite (CRRES). They documented the convection electric field penetration to low invariant latitudes in both the ionosphere and magnetosphere. Convection electric field boundaries were close to the inner edge of the ring current (identified from  $< 30$  keV ion observations by the CRRES LEPA instrument) throughout the main and early recovery phases of the storm but twice penetrated to L values Earthward of this inner edge. During periods of effective ring current shielding, the most-Earthward penetration of these fields should coincide with the inner edge of the ring current [*Harel et al.*, 1981].

During the June 1991 storm, electric potentials at subauroral latitudes (earthward of the auroral electron precipitation boundary) made up large fractions of the total electric potential across the afternoon convection cell. These subauroral (penetration) potentials sometimes reached values as high as 60 kV, as seen by the DMSP and CRRES satellites [e.g., *Burke et al.*, 1998]. Embedded within broad regions of strong subauroral electric fields were narrower ( $\sim 1^\circ$  latitude) structures identified as subauroral ion drift (SAID) events, where fields up to 100 mV/m were observed. *Garner* [2000] utilized these data as ground-truth for a simulation of the June 1991 magnetic storm using the Rice Convection Model (RCM). On the basis of calculated ion drifts, the RCM solves for magnetospheric particle distributions, currents into and out of the magnetosphere, and the electric field potential pattern in the magnetosphere. For simplicity and

computational considerations, the RCM study neglected ring current collisional losses and treated only a proton ring current.

Using the Rice Convection Model, *Garner* [2000] found that shielding was weak throughout this storm with frequent electric field penetration to low L values. In addition, he found that plasma sheet density and temperature affect the strength and location of the shielding electric fields. Higher density plasma sheets create stronger shielding fields because of the increase in the number of charge carriers. Lower temperature plasma sheets (with plasma sheet pressure held fixed) are more effective for two reasons: (1) at fixed pressure, lower temperature implies higher density and more charge carriers and (2) lower-energy plasma can penetrate more deeply into the inner magnetosphere resulting in greater adiabatic acceleration and stronger currents closing through the subauroral ionospheric conductivity gradients and thus more intense penetration fields.

In the present study, we do not directly calculate the effects of the penetration electric field but adopt a modified *McIlwain* [1986] electric potential to specify the large-scale field in the RAM model [*Liemohn et al.*, 2001a]. The McIlwain field model was used because it has many realistic features, including: a non-dusk-fixed stagnation point, dawn-dusk and noon-midnight asymmetries, and an enhanced radial electric field intensity in the post-midnight sector (which is in agreement with radar observations [c.f., *Senior et al.*, 1989]). The McIlwain magnetospheric electric potential description [*McIlwain*, 1986], inferred from geosynchronous particle data, has the form

$$\Phi_{Mc} = \kappa H \left[ R(E_y \sin \varphi + E_x \cos \varphi) + \Phi_{off} \right] \quad (4)$$

For this study, the strength term  $\kappa$  has been made proportional to the cross polar cap potential difference.  $E_y$ ,  $E_x$ , and  $\Phi_{off}$  are all constants determined empirically by matching geosynchronous dispersion signatures [*McIlwain*, 1986]. The shielding factor  $H$  is given by

$$H = \frac{1}{1 + (R_0/R)^8}$$

and is dependent not only on  $R$  (as with the Volland-Stern shielding factor) but also on  $\varphi$  and magnetic activity ( $K_p$ , in this case)

$$R_0 = 0.8[9.8 - 1.4\cos\varphi - (0.9 - 0.3\cos\varphi)K_p]$$

This yields a shielding region with several distinct features: (a) the shielded region is azimuthally asymmetric with a smaller nightside extent than on the dayside (low  $K_p$ ), (b) the shielding region gets smaller with  $K_p$ , and (c) the shape reverses for  $K_p \geq 5$ , with less shielding on the dayside than on the nightside (emulating faster shielding recovery on the nightside than on the dayside). These are very similar to trends seen in self-consistent calculations of the shielding and penetration electric field from the Rice Convection Model [*Jaggi and Wolf, 1973; Wolf et al., 1982; Garner, 2000*]. Therefore, it is expected that this modified *McIlwain* [1986] model should yield a reasonable result for the energetic ions in the inner magnetosphere. However, it is an empirically-derived analytical description that does not take into the account the actual partial ring current-induced electric field, and so uncertainties and inaccuracies exist in the model results. For more details on this field description, see *Liemohn et al. [2001a]*.

To achieve higher time resolution in the convection potential than provided by the standard 3-hr  $K_p$  index, a synthetic  $K_p$  index is calculated from the Air Force Research Laboratory (AFRL) midnight auroral boundary index (MBI) using a statistical relationship presented by *Gussenhoven et al. [1983]*. The MBI is the magnetic latitude of the equatorward edge of the diffuse aurora at midnight. The diffuse aurora is produced by the precipitation of plasma sheet electrons into the ionosphere; therefore, the MBI tracks the inner edge of the plasma sheet. The cross polar cap potential, used to scale the strength of the convection potential for this simulation, is obtained from the assimilative mapping of ionospheric electrodynamics (AMIE) technique [*Richmond and Kamide, 1988*]. The top 4 panels in Figure 3 give the polar cap potential drop from the AMIE model, the MBI index, the MPA nightside plasma sheet density, and the strength of the modeled convection electric field at geosynchronous orbit ( $L = 6.6$ ) at midnight.

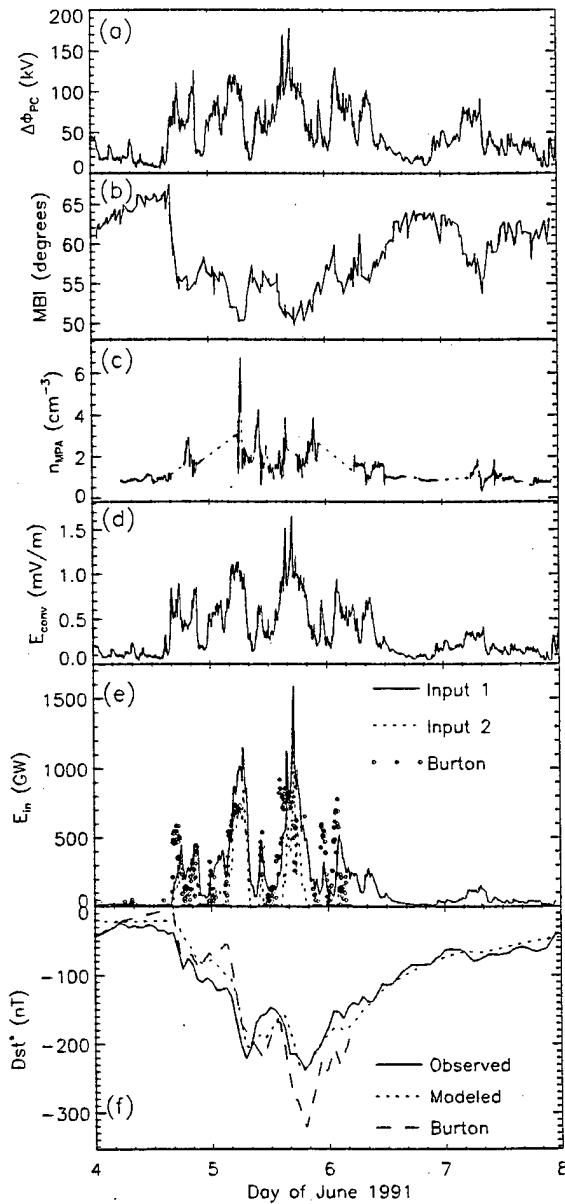


Figure 3. Plot of (a) the cross polar cap potential drop calculated from the AMIE technique, (b) the midnight auroral boundary index (MBI), (c) nightside MPA densities, (d) convection electric field at geosynchronous orbit at local midnight, (e) energy input functions to the simulation (see text) and from the *Burton et al. F(E)* relation, and (f) observed and modeled  $Dst^*$ , along with the  $Dst^*$  prediction from the Burton formula.

## 4.2. Nightside Plasma Sheet Source Population

The boundary conditions for the simulation are obtained from geosynchronous observations of the nightside plasma sheet, taken from within  $\pm 4$  hours of midnight. As described above in Section 2.2, two geosynchronous satellites (1989-046 and 1990-095) were making observations of the plasma sheet during the June 1991 magnetic storm. They were located at  $195^\circ$  E and  $97.5^\circ$  E longitudes, respectively. The 6.5 hour separation of the satellites in local time provides almost continuous coverage of the nightside plasma sheet within  $\pm 4$  hours of midnight for 14.5 hours out of every day, followed by an  $\sim 9.5$  hour gap in coverage. 1989-046 provides boundary conditions from 7 UT (20 hrs MLT) until 15 UT (4 hrs MLT) each day. Just before 1989-046 exits the nightside plasma sheet on the dawnside, 1990-095 enters this region on the duskside at 13.5 UT (20 hrs MLT) until 21.5 UT (4 hrs MLT). From 21.5 UT until 7 UT the next day there is no satellite in the nightside plasma sheet. For the purposes of creating a boundary condition for the ring current simulation, variations in the observed plasma sheet density are taken to represent temporal variations of a spatially uniform nightside plasma sheet. The data gaps created by the incomplete satellite coverage are filled in as much as possible by using electron observations from later local times or ion observations from earlier local times if it appears that the satellite is in a relatively fresh plasma sheet (not significantly degraded by losses). Electron plasma sheet observations are used only to infer the plasma sheet ion density, with the ion temperature taken to be as measured. If neither satellite produces suitable measurements, the source properties are obtained by a linear interpolation between the last and next valid data points.

Figure 4 displays density and temperature moments derived from the MPA observations throughout the storm interval.  $Dst^*$  is replotted in Figure 4a for reference purposes. The methods for deriving these moments are described by *Thomsen et al.* [1999]. A complete 3D distribution is obtained over a 10-sec spin period once every 86 seconds. As mentioned previously, the MPA instrument measures only energy per charge so the moments calculation

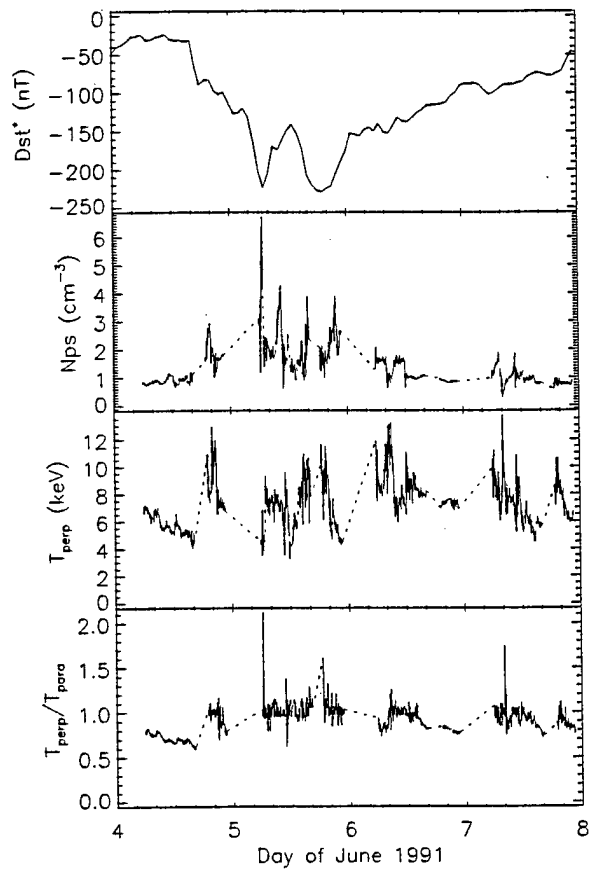


Figure 4. Plot of (a) pressure-corrected Dst, (b) nightside plasma sheet density, (c) nightside plasma sheet  $T_{\perp}$  and (d) nightside plasma sheet  $T_{\perp}/T_{\parallel}$ .

assumes all positively charged particles are protons. Figure 4b shows the variation in the nightside geosynchronous plasma sheet density  $N_{ps}$  under this assumption. During the complex main phase development, the density is enhanced and has considerable structure, with peaks reaching values between  $4 \text{ cm}^{-3}$  and  $7 \text{ cm}^{-3}$ . The perpendicular temperature (Figure 4c) is lower overall during the main phase development. Figure 4d gives the ratio between perpendicular and parallel temperatures in the plasma sheet source population. During the main phase the populations tend to be more isotropic (i.e., ratio of perpendicular to parallel temperature tends toward 1).

The assumption that all ions, measured by MPA, are protons becomes increasingly inaccurate during the main phase of large magnetic storms such as this event. *Young et al.* [1982] derived a parametric formula, based on observations at geosynchronous orbit, which gives composition as a function of solar activity (as represented by F10.7 cm flux) and magnetic activity (as represented by the MBI-derived  $K_p$  value). This formula is used to estimate the composition of the MPA fluxes and to correct the density moments to take into account heavy ion components of the flux. The actual nightside plasma sheet density is therefore higher than that shown in Figure 4b. The percentage  $O^+$  composition at energies  $> 50 \text{ keV}$  (exceeding the MPA energy range) is assumed to be an exponentially decreasing function of energy. The appropriateness of this assumption is tested after the fact by comparison of model distributions to CRRES/MICS observations with reasonable agreement.

### 4.3 Energy Input Function

Modeled energy input into the ring current region has two components: (1) energy inflow at the nightside outer boundary ( $L=6.7$ ) and (2) the adiabatic acceleration/deceleration of particles as they move along drift paths within the model volume. The energy input in the model is calculated independently of upstream solar wind parameters using observations of the nightside plasma sheet distributions (Section 4.2) and velocities derived using reasonable models of the large-scale electric field configuration (Section 4.1). The energy input can also be

independently estimated from the observed upstream solar wind parameters, combined with statistically-derived ring current decay lifetimes [e.g., *Burton et al.*, 1975]. Such statistical energy input functions have had remarkable success in predicting the strength of the ring current during magnetic storms [see review by *Gonzalez et al.*, 1994]. Figure 3e is a comparison between our modeled energy input function(s) and the *Burton et al.* [1975] energy input function, given by

$$F[\text{GW}] = \begin{cases} -1.68 \cdot 10^{-2} (E_y - 0.5) & E_y > 0.5 \text{ mV/m} \\ = 0 & E_y \leq 0.5 \text{ mV/m} \end{cases} \quad (5)$$

Note that 1 GW is equivalent to 0.894 nT/h, using the DPS relation (3) to convert kinetic energy input into a magnetic depression change. Figure 3e displays two versions of the model energy input function. Both contain the adiabatic energization of particles within the model volume, but Input 1 (solid line) includes only the energy input through the nightside outer boundary, while Input 2 (dotted line) includes the difference between the inflow of energy on the nightside and the outflow on the dayside. The energy flux and number flux exiting the model volume on the dayside is calculated using the convection velocities and plasma distributions in the outermost cell across the dayside from 0600 MLT to 1800 MLT. Overplotted is the *Burton et al.* energy input function,  $F$  (symbols). The values from (5) are only shown through the period of valid solar wind data, cutting off early on June 6. There is quite good agreement between the maximum values of Input 2 and  $F$  during the main phase development of the ring current on June 5. Input 1 reaches much higher values than  $F$ . Agreement with Input 2 (rather than Input 1) is expected because the *Burton et al.* [1975]  $Dst^*$  prediction algorithm includes a loss term proportional to  $Dst^*$  that essentially represents the dayside outflow and charge exchange losses of the ring current. The correspondence between  $F$  and the model energy inputs degrades significantly during the recovery phase. There are several peaks in  $F$  that are not reproduced in the model. Presumably the energy input reflected in  $F$  is related to auroral processes at this point and is not being deposited in the ring current.

The loss term in the Burton formula contains a constant decay rate of 7.7 hours. This is a good average value of the decay rate (it was found through fitting Dst recoveries) but is unable to represent all events. To illustrate this point, the prediction of Dst\* from the *Burton et al.* [1975] method is given in Figure 3f along with the observed Dst\* and our modeled Dst\* indices for reference. It can be seen that the Burton formula did not replicate the observed value, recovering too quickly from the first peak (on June 4), missing the timing of the second peak (early on June 5), and overpredicting the magnitude of the third peak (late on June 5). One explanation is that the Burton formula only depends on the solar wind  $E_y$  value (and on the previous value of Dst\*) and does not take into account any information from the near-Earth plasma sheet (the strength of the ring current source population) in deriving the energy input. In addition, the loss timescale (which is calculated in our ring current model) is shorter than 7.7 hours during the main phase and early recovery periods. A recent statistical study by *O'Brien and McPherron* [2000] found faster loss time scales than *Burton et al.* and, furthermore, these time scales decreased with increasing solar wind  $E_y$  values. A fast loss timescale with an  $E_y$  dependence is consistent with outflow of ring current particles through the dayside magnetopause (a process that depends on convection strength) being the dominant loss process during this part of the storm [*Liemohn et al.*, 1999]. No other identified ring current loss process can account for a globally-averaged timescale of less than 7.7 hours.

## **5.0 Simulated Ring Current: Detailed View**

### **5.1 Ring Current Characteristics**

Plate 3 gives a summary of ring current characteristics extracted from the simulation of the June 1991 magnetic storm. Shown at selected times during the simulation are parallel and perpendicular currents and total energy density in the equatorial plane with the sun to the left, midnight to the right, and dusk to the bottom of each dial plot (a view from over the north pole).

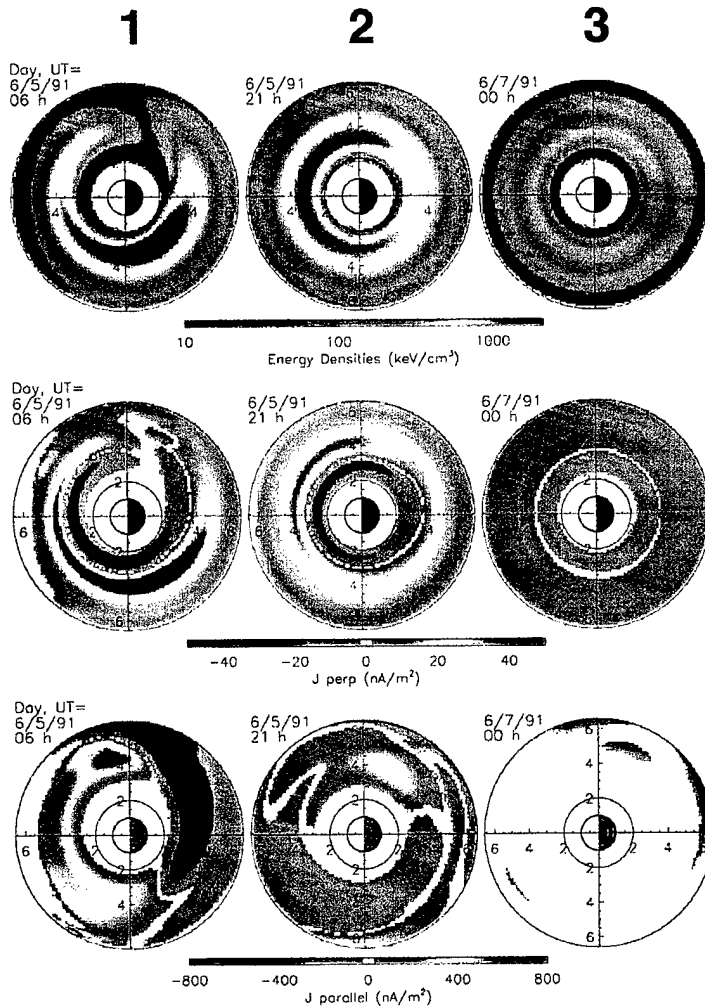
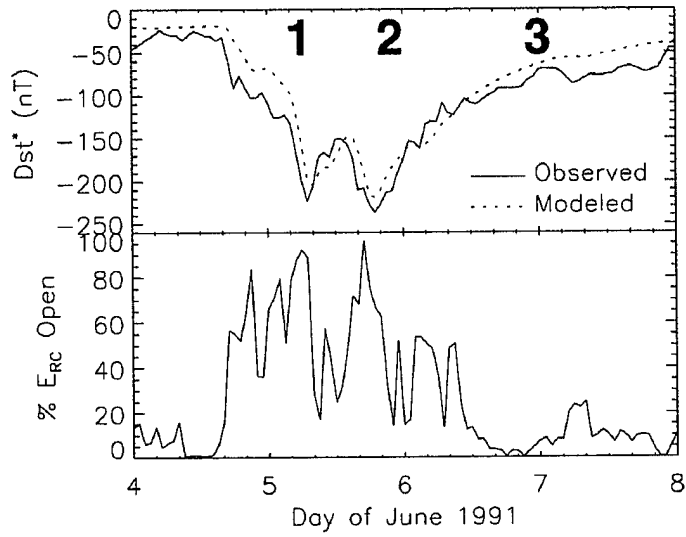


Plate 3. Dial plots of ring current pressure (energy density) in the equatorial plane, perpendicular current density in the equatorial plane, and parallel current density into the northern hemisphere ionosphere (120 km altitude). Also plotted is observed and modeled  $Dst^*$ , for reference, and the percentage of ring current energy  $E_{RC}$  carried by ions on open drift paths.

Times during the second and third ring current intensifications and well into the late recovery phase were selected to illustrate important features in the ring current development.

During the main phase (time 1), the ring current is highly asymmetric as seen in the energy density. The bulk of the ring current is on open drift paths, which intersect the dayside magnetopause. In the late recovery phase (time 3), the ring current becomes symmetric in local time. During the early recovery phase (time 2), the ring current is gradually transitioning from an asymmetric (open drift paths) to a symmetric (trapped) configuration. The ring current is beginning to look more symmetric but there is still a significant partial ring current component as indicated by the presence of significant field-aligned currents (bottom row). The perpendicular currents in the magnetosphere are shown in the middle set of dial plots in Plate 3. In the main phase and early recovery phase, these currents are asymmetric in local time, and their divergence gives the field-aligned (or region II) portion of the partial ring current loop (shown in the bottom set of dials in Plate 3). These field-aligned currents are quite strong and complex during the main and early recovery phase (times 1 and 2). By the late recovery phase (time 3), the partial ring current has largely disappeared, leaving a symmetric ring current which consists of only a non-divergent component. The dominance of the partial ring current during the main and early recovery phase, its direct connection along open drift paths to the magnetotail and its conversion to a symmetric ring current only in the late recovery phase are clearly seen.

Also shown at the top of Plate 3 is the percentage of ring current energy carried by ions on open drift paths. It is seen that this quantity peaks at values above 90% for the second and third injections (during the main phase of each one). It then sharply recovers after its peak, with large swings to values below 20% and back up to 50% or more. Because this value measures the instantaneous drift path of the ions, it is highly dependent on the cross polar cap potential. Northward turnings of the IMF cause sudden reductions in the potential difference and therefore also in this value of the percent of energy on open drift paths. Thus, this quantity is actually a lower limit on the asymmetry of the ring current, because the distribution can still be asymmetric even after its capture in the inner magnetosphere. This persisting asymmetry and later

evacuation of the material is seen in the subsequent peaks of the percent-open quantity to values over 50% early on June 6.

The results of Plate 3 can be viewed in light of the magnetic field calculations from the symmetric and asymmetric ring currents recently performed by *Tsyganenko* [2000]. Integrating the current densities yields values of the symmetric and asymmetric components of the ring current during the storm main phase that are quite different from those assumed by *Tsyganenko* [2000]. In that study, the symmetric ring current was assumed to have a peak current density of a few nA/m<sup>2</sup> around L=3.5 (plasma pressure peaked at L=2.8) with a total azimuthal current of 0.75 MA. The asymmetric ring current was assumed to have a peak current density of just over 1 nA/m<sup>2</sup> around L=7 (plasma pressure peak at L=6) with a total azimuthal current of 0.7 MA. In the simulation results of the present study, the symmetric ring current begins below 1 MA, but rises up to nearly 10 MA during the partial recovery of the ring current following each injection event. The calculated partial ring current spikes up to 15 MA during the main phases of the two large injections on June 5. Furthermore, the locations of the symmetric and asymmetric ring currents are different between the two studies, with the both the symmetric and asymmetric ring currents peaked near L=4. For more details on the stormtime current distribution, see *Liemohn et al.* [2001b]. These discrepancies are not surprising, since *Tsyganenko* [2000] used the quiet time ring current ion distributions of *Lui and Hamilton* [1992], and the present study is examining a strong storm. Therefore, the results from that study and this one are not inconsistent.

## 5.2 Comparison with Satellite Observations

To quantify how well the model reproduces observations, simulation results are compared to satellite observations at selected locations. Figure 5 shows this comparison for 3 inbound passes (post-dusk local time) of the CRRES satellite (during storm growth, early recovery, and late recovery). Presented here is ion energy density as a function of position (L shell) for the two main ring current species of H<sup>+</sup> and O<sup>+</sup>. The measured values are from the MICS instrument [c.f., *Roeder et al.*, 1996b], and are integrated over energies above 40 keV for

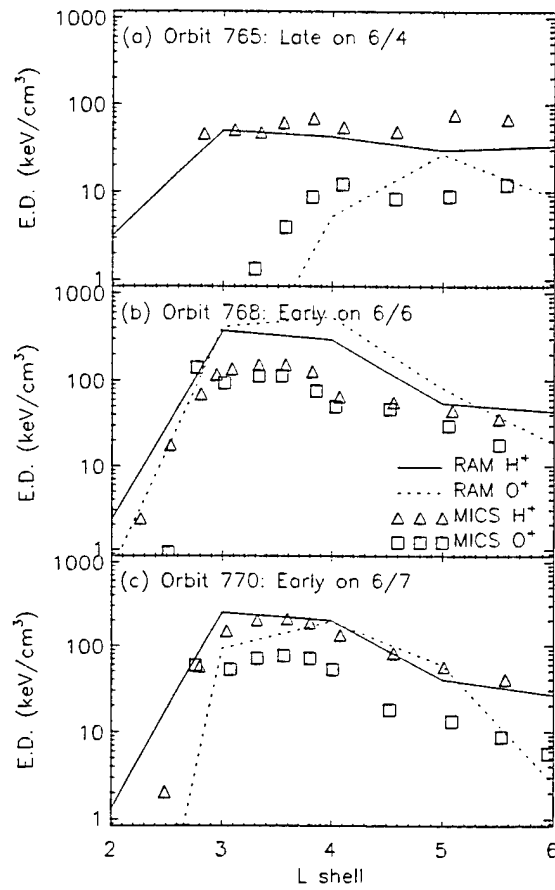


Figure 5. Energy densities observed by CRRES MICS and simulation results for the same times and locations for 3 outbound passes of the spacecraft. Times are (a) during the growth phase, (b) during the early recovery phase, and (c) during the late recovery phase. MICS data are from *Roeder et al.* [1996b].

each species. The model results have been integrated over the same energy range. It is seen that there is excellent agreement between the model results and the measured values in Figures 5a and 5c, for both species but particularly for  $H^+$ . In Figure 5b, the model results are slightly higher than the measured values. There are several reasons why this could be the case. The first is that the plasma density applied at the outer boundary might have been too large. This time is in the middle of a data gap in the LANL boundary condition (Figure 4), and the real input distribution could have been different from the assumed one. A second reason is that our modeled electric field could be too strong at this time. This would drive the particles deeper into the magnetosphere, enhancing their energy and creating a stronger ring current. A third explanation is the lack of a self-consistent penetration electric field in the calculation. The exact influence of this field on the energetic ions is unknown, but because the ExB drift is expected to be in the sunward direction at this location (evening sector), it would drive these high-energy ions in the same direction as the gradient-curvature drift. Such an enhancement in flow might accelerate the removal of the main phase ion distribution, which is clearly more intense than the recovery phase distribution, and thus the omission of this field might delay the recovery to lower flux levels.

## **6.0 Simulated Ring Current: Globally-Integrated View**

### **6.1. Multi-Stage Dst\* Development**

As mentioned previously, the June 1991 magnetic storm had a complicated multi-stage main phase development with three major intensifications. As discussed in the introduction, there are a number of interesting issues associated with multi-step Dst storms that motivate an investigation of this feature. The main issues are: (1) does a pre-existing ring current from earlier intensifications during the storm significantly influence the strength of the ring current in subsequent intensifications, (2) does the overall length of the complex main phase development affect the maximum strength of the ring current (complex storms tend to have longer main

phases), (3) are changes in the plasma sheet density (possibly due to preconditioning by earlier intensifications) the key element in modulating the strength of the ring current during intensifications, and (4) how important are changes in the convection strength?

Figure 3 shows that the peak energy inputs during the three major storm minima are successively larger. This is true for both the Burton formula and for our model inputs (1 and 2). For both estimates, it is primarily attributable to progressively larger values of  $E_y$  (Figure 1e) caused by progressively stronger southward IMF (Figure 1d). In addition to the changes in the convection electric field, the model energy input is strongly dependent on the variations in the density of the plasma sheet population. Plasma sheet densities reach maximum values during the second intensification and drop off again before the third. The magnitude and variability of the RAM model energy input function is strongly affected by these density changes to the point that approximately equal integrated energy inputs are achieved during the second and third intensifications despite the differences in the convection electric field. This was not true for the Burton et al energy inputs based only on the solar wind  $E_y$  (Figure 3e).

To examine the impact of a pre-existing ring current population, each intensification is simulated as an isolated storm. For this investigation, previous intensifications are removed by replacing the input functions (solar wind parameters, geophysical indices, and nightside plasma sheet inputs) for a given block of time with the last values they had prior to the deleted interval. This ensures that all of the input parameters remain constant throughout the omitted interval, and the ring current is essentially in a slow-decay phase during which very little activity occurs. Figure 6 presents the results of 3 model runs: (1) including all 3 injections (solid line, as shown in previous figures); (2) with the first injection removed (all input values from 1600 UT to 2200 UT on June 4 replaced with the 1600 UT values) (dotted line); and (3) with both the first and second injections removed (all input values from 1600 UT on June 4 to 1200 UT on June 5 replaced with the 1600 UT values) (dashed line).

Figure 6 demonstrates that preconditioning of the inner magnetosphere by a previous intensification is not particularly important in creating a stronger intensification later in the

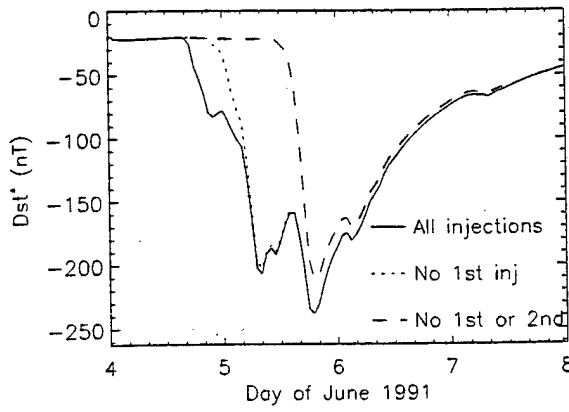


Figure 6. Modeled Dst\* from simulations, including all of the injection intervals (solid line), only the second and third injections (dotted line), and only the third injection (dashed line).

storm. In fact, 98% of the second Dst minimum (and 100% of the third) was reproduced when the first injection was removed. Removal of both the first and second injections reduced the strength of the third injection to 89% of its full value. Without the small (11%) contribution from the previous intensification, the 3rd Dst\* minimum is similar in strength to the 2nd Dst\* minimum. This reflects the fact that the model integrated energy inputs for these two injections are approximately equal. The small fraction of the particles from the second injection that remain during the third injection produce a slightly more intense ring current. The removal of pre-storm populations during the initial ring current build up was also seen in Rice Convection Model results for the same storm interval [Garner, 2000].

Examination of the ion drift trajectories within the inner magnetosphere further illustrates why a pre-existing ring current does not significantly influence subsequent intensifications in the model. Using the method described by *Liemohn et al.* [2001a], instantaneous maps of the percentage of ions on open drift paths were produced at intervals throughout the simulation. If these drift trajectories remain open for sufficient time, the ions on them will drift to the dayside magnetopause and be removed from the inner magnetosphere. Conversely, if significant ring current energy populations remain on closed drift paths throughout the main phase development, then they should contribute to subsequent intensifications of the ring current. During all 3 intensifications, the percent of the total ion energy on open drift paths exceeds 80%. This indicates that nearly all of the ring current is a partial ring current, and that most of the ions will only make one pass through the inner magnetosphere. This includes the ions in the peak of the ring current, around dusk near  $L=3.5$  in the 25 to 75 keV energy range. All of these particles are on open drift paths. Furthermore, their drift time to convect from the dusk meridian to the dayside simulation outer boundary (geosynchronous orbit) is, on average, less than 6 hours. Because the Dst minima are more than 6 hours apart, most of the particles are swept out of the inner magnetosphere before the subsequent intensification.

In summary, a number of insights into multi-step Dst storms are possible from the simulation of the June 1991 event. For this case, the first intensification of the ring current is

largely swept out of the magnetosphere on open drift trajectories and does not serve to precondition or amplify the strength of the ring current when the second southward IMF interval impacts the magnetosphere. The integrated energy inputs for each intensification are consistent with the relative amplitudes of the Dst minima in each case, similar to the *Chen et al.* [2000] study that found model storms with the same integral input produce storms of similar size. The energy inputs are strongly dependent on both the changes in the convection electric field and the large variations in the plasma sheet densities that occur throughout the event. If there is a preconditioning element operating in multi-stage ring current intensifications, it is more likely through the preconditioning of the plasma sheet population by upstream solar wind and ionospheric coupling [c.f. *Kozyra et al.*, 1998a]. Exactly how variations in the plasma sheet density are related to upstream and internal magnetospheric conditions is not clear but is important to our understanding of the geoeffectiveness of solar wind drivers. When the Dst\* is predicted based on upstream solar wind  $E_y$  alone and statistical decay time scales as in the Burton et al. formulation, the relative sizes of the minima are not reproduced (see Figure 3f).

## 6.2 Two-Phase Decay

Studies indicate that the rapid time-scales for ring current decay in phase 1 of a two-phase decay are due to flow out at the dayside magnetopause of ring current particles on open drift paths in the presence of declining plasma sheet densities [*Ebihara and Ejiri*, 1998, 2000; *Liemohn et al.*, 1999, 2001a]. These open drift paths are subsequently converted to closed drift paths as the convection electric field weakens. The remaining trapped ring current particles decay mainly through charge-exchange collisions with the geocorona, which is a much slower process. The dramatic difference in time-scales between flow-out at the dayside magnetopause and charge exchange collisions accounts for the two-phase decay which is typically seen during the recovery phase of major magnetic storms.

These earlier studies involved simulations of storms during solar minimum conditions. The June 1991 storm occurred during solar maximum conditions and contained a considerably

larger oxygen ion component than previous simulations of the two-phase decay. Results of this study confirm the gradual changeover between flow-out losses and charge-exchange losses in producing two-phase decay. However, a number of modifications to this simple picture occur during the June 1991 storm.

Figure 7a gives the observed Dst\* profile (solid line), the modeled Dst\* due to H<sup>+</sup> (dashed line), due to O<sup>+</sup> (dash-dot line) and the total from both species (dotted line). It is clear that O<sup>+</sup> makes the major contribution to the modeled Dst\*. To compare this contribution to the observations, it is useful to split the results according to spatial location. For instance, *Roeder et al.* [1996b] (hereinafter Roeder) split the CRRES orbit into two zones, L=3-5 and L=5-7, to show the difference in composition between the inner and outer ring current regions. Similarly, *Daglis* [1997] (hereinafter Daglis) examined only the measurements in the L=5-7 portion of the CRRES orbit. Figures 7b and 7c show a data-theory comparison of these published energy density composition percentages from CRRES/MICS observations (symbols) with the corresponding model results for the full ring current energy range (solid lines) and for the truncated energy ranges (dotted lines) covered by the observations. Note that the energy range of comparison is E>40 keV for the Roeder and solid-line model results and E>50 keV for the Daglis results. Both of these data analysis procedures reduced the data from half of a satellite orbit (within the L band of interest) into a single value for the O<sup>+</sup> content, and so the spacing of the data-derived percentages are at least several hours apart.

The two CRRES values (Roeder and Daglis) are determined through distinctly different methods. To obtain estimates of the ring current energy density from CRRES, *Roeder et al.* [1996b] used in-situ CRRES observations in the local dusk to midnight sector in a restricted latitude range close to the equatorial plane (no effort was made to map fluxes to the equator). This was done in an attempt to separate magnetic latitude and temporal variations in the composition. This method, however, resulted in significant data gaps throughout the storm (particularly during the main phase development of the storm on June 5) when CRRES moved to higher magnetic latitudes. *Daglis* [1997] estimated composition from the CRRES data for this

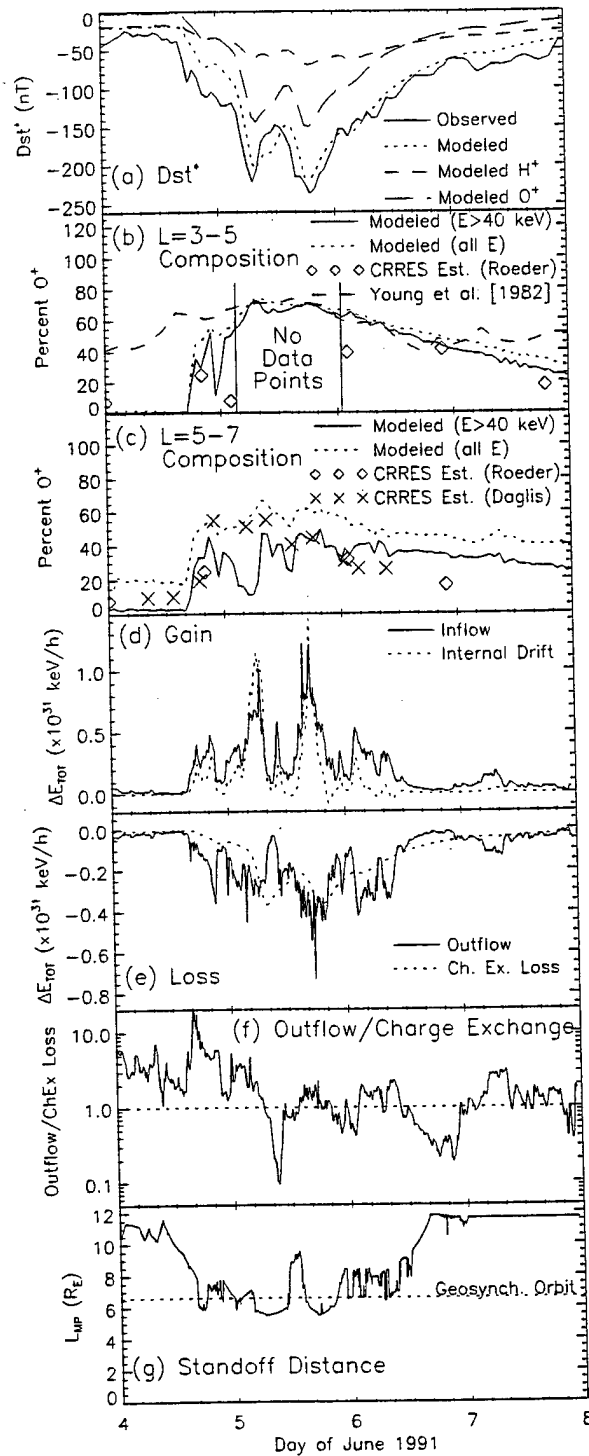


Figure 7. (a)  $Dst^*$  from observations, from the model results, and from each of the species ( $H^+$  and  $O^+$ ) individually. (b)  $O^+$  contribution to ring current energy density in the  $L = 3-5$  belt calculated from the model results (solid line,  $E > 40$  keV; dotted line, all energies) and estimated from the CRRES measurements from *Roeder et al.* [1996b] and *Daglis* [1997] (symbols and crosses, respectively). (d) Total energy input rates from the simulation results from inflow through the boundary and net adiabatic drift effects. (e) Total energy loss rates from the simulation results from outflow through the boundary and charge exchange. (f) The ratio of the outflow loss rate to the charge exchange loss rate (the two quantities in the panel above), with a dashed line at unity for reference. (g) The subsolar magnetopause location (standoff distance) as computed by the *Shue et al.* [1998] formula.

storm period under different assumptions to correct for MLAT variations, therefore using a larger portion of the data set for his analysis. Both methods, however, contain large uncertainties, but their extent is unknown and therefore no error bars are drawn on the data points.

For the L=3-5 region, the > 40 keV energy range contains the bulk of the ring current ion population, and thus the two model result curves (one for E> 40 keV and one for all energies) are very similar. In addition, the model O<sup>+</sup> percentage compares favorably with observations of this quantity from Roeder.. A striking feature of Figure 7b is that the model ring current composition throughout the main and early recovery phase closely follows the composition of the plasma sheet source population at the outer boundary specified by the *Young et al.* [1982] formula (dashed line). This is because the ring current is largely on open drift paths (see Plate 3) during this time providing a direct connection between ring current and plasma sheet populations. During the late recovery phase, the ring current composition at L=3-5 diverges significantly from the outer boundary composition as drift paths become dominantly closed. Superimposed on this overall behavior are two intervals in the main and early recovery phase during which the IMF turned abruptly northward, temporarily trapping the ring current on closed drift paths and increasing the relative importance of charge exchange loss. These intervals are clearly visible in Figure 7f centered at ~9 UT on June 5 and ~0 UT on June 6. There are small decreases in the O<sup>+</sup> percentage at E> 40 keV near the ring current peak (Figure 7b) associated with each of these intervals, but as soon as the IMF turns southward and drift paths become open again, the ring current composition returns to that of the plasma sheet source population.

However, for the L=5-7 region (Figure 7c), the E > 40 keV range is typically well above the characteristic energy of the hot ions (compare with Figure 4, measured at L=6.6). Therefore, the solid line in Figure 7c reflects the composition of the high-energy tail of the ion distribution imposed at the outer boundary. The assumption was made that oxygen decreased exponentially above 50 keV energies in the inner plasma sheet (outer boundary of the model); while protons were given by measurements from the SOPA instrument on the LANL geosynchronous

satellites. During the main phase of the storm (late June 4 and June 5), a comparison with CRRES observations at  $L=5-7$  indicates that the model underestimates the oxygen content at high energies near the outer boundary of the model, but that the oxygen content averaged over all energies agrees fairly well with observations for this time period. However, the underestimate of the  $O^+$  percentage at  $E > 40$  keV in the ions at the outer boundary does not significantly impact the composition of the main part of the ring current at lower  $L$  values ( $L=3-5$ ) which is formed dominantly from the lower energy portion ( $<50$  keV) of the outer-boundary plasma sheet ions. In the range  $L=3-5$ , there is very good agreement between predicted and observed oxygen content. Therefore, the *Young et al.* [1981] empirical formula for the plasma sheet composition at geosynchronous orbit seems to be a good description of the true composition for the  $E < 40$  keV portion of the distribution at all times and is also a good description for the  $E > 40$  keV portion of the distribution during stormtime injections.

The next three panels of Figure 7 are important for understanding the sources and losses that drive the global ring current. Figure 7d displays the globally-integrated energy gains due to particle drifts in through the model boundaries (solid line) and net adiabatic energization within the model volume (dotted line). It is seen that while energy inflow into the simulation domain is usually the larger value, these two energy sources are roughly comparable for this storm. In general, the adiabatic energization has a similar time profile to the energy inflow rate, but is slightly delayed and can even be negative (net energy loss) at times.

Figure 7e shows globally-integrated energy losses due to particle drifts out through the dayside magnetopause (solid line) and charge exchange (dotted line). Note that other loss processes were included in the calculations, but these are the two most significant ones. The ratio of outflow losses to charge exchange losses is shown Figure 7f. As in previous simulations, losses due to drifts out the dayside magnetopause (solid line) dominate during the main phase. For this storm the 3-phase decay is clearly seen reflected in the ratio of charge-exchange to flow-out loss. At the very beginning of the ring current recovery during the northward IMF interval, charge-exchange briefly dominates the losses. The IMF again swings southward triggering an

interval of mostly flow-out loss which constitutes phase 1 of a characteristic 2-phase decay. When phase 2 begins at ~12 UT on June 6, drift losses become small and charge exchange losses dominate the decay. One difference between this event and previous solar minimum storm simulations [Liemohn *et al.*, 1999, 2001a] is that charge exchange losses are significant in the early decay. The combination of drift and rapid charge exchange losses will decrease the decay time scales during the early recovery phase over those due to drifts alone. From 20 UT on June 5 to 12 UT on June 6 (when convection subsides), 53% of the total loss of ring current energy was due to flow-out through the dayside magnetopause.. This is because the early recovery phase can actually be divided into two intervals, one dominated by charge-exchange loss and the other by flow-out loss. -

Finally, the magnetopause location calculated from the *Shue et al.* [1998] model, which includes the effects of solar wind dynamic pressure as well as reconnection, is shown in Figure 7g. Geosynchronous orbit is marked for reference (dotted line). The magnetopause was compressed and eroded inside geosynchronous orbit for two approximately 6-hour intervals during the storm (see also Section 2.3). During the second interval, significant additional loss of ring current ions occurred (see Figure 7e) as particles, drifting to the dayside on open drift paths, encountered the magnetopause at low L values. Such an additional loss was also proposed for the February 1986 great magnetic storm [Kozyra *et al.*, 1998b]. This type of loss may limit the development of strong ring currents during storms where high solar wind dynamic pressure occurs during the main phase. It is interesting to note that in the interval ~8-12 UT on 5 June, during which the magnetosphere was compressed inside geosynchronous orbit the outflow losses actually decreased. During this interval a northward turning of the IMF caused a partial recovery of the ring current, reducing convection strength and thus outflow losses.

### **6.3 Correlation between Composition Changes and Dst**

*Daglis* [1997] presented observations from 4 large and 1 moderate storm during the CRRES mission, including the 4-6 June 1991 storm. In all cases, the O<sup>+</sup> contribution to the

energy density and the Dst index changed in parallel. An enhancement of the ring current in the main phase is concurrent with an increase in the percentage  $O^+$  contribution. A decline in activity triggers ring-current decay and produces an immediate decline in the percentage  $O^+$  contribution to the energy density. In fact, during the great magnetic storms of 24 March 1991 [Daglis, 1997] and February 1986 [Hamilton *et al.*, 1988], the two-phase decay in the Dst index was also present in the declining  $O^+$  percentage.

The June 1991 simulation offers a natural explanation for the close correspondence between percentage  $O^+$  and Dst. Plate 4 displays a line plot of percentage  $O^+$  at dusk along with a plot of Dst\* for reference. Four selected time intervals are marked on this plot, including (1) the initial rapid increase in  $O^+$  concurrent with the Dst decrease, (2) the evolution during the main phase, (3) the rapid changes during the early recovery phase and (4) the slowly declining percentage in the late recovery phase. The dramatic composition changes that occur result from the change in composition of the plasma-sheet source population. During the increase in magnetic activity that triggers the onset of the storm, the source population at geosynchronous orbit becomes enriched in oxygen [Young *et al.*, 1982]. This source population has immediate access to the inner magnetosphere along open drift paths (see dial plots for interval 1 in Plate 4). Increasing oxygen percentages in number density appear first along the nightside outer boundary of the model, and then move through the inner magnetosphere. As peak activity levels are reached during the storm main phase (Interval 2 in Plate 4), high oxygen percentages appear in the source populations at the outer boundary and propagate into the inner magnetosphere. During the rapid decrease in magnetic activity following the main phase, increasingly oxygen-poor plasma sheet source populations sweep through the inner magnetosphere on open drift paths which are gradually being converted to closed drift paths; the more oxygen-rich populations, associated with the main phase plasma sheet source, are being lost at the dayside magnetopause (see Interval 3 in Plate 4). This transition from relatively oxygen-rich to oxygen-poor plasma occurs throughout the early recovery phase. In the late recovery phase (Interval 4 in Plate 4), the symmetric ring current, which is by that time relatively oxygen-poor, decays slowly through

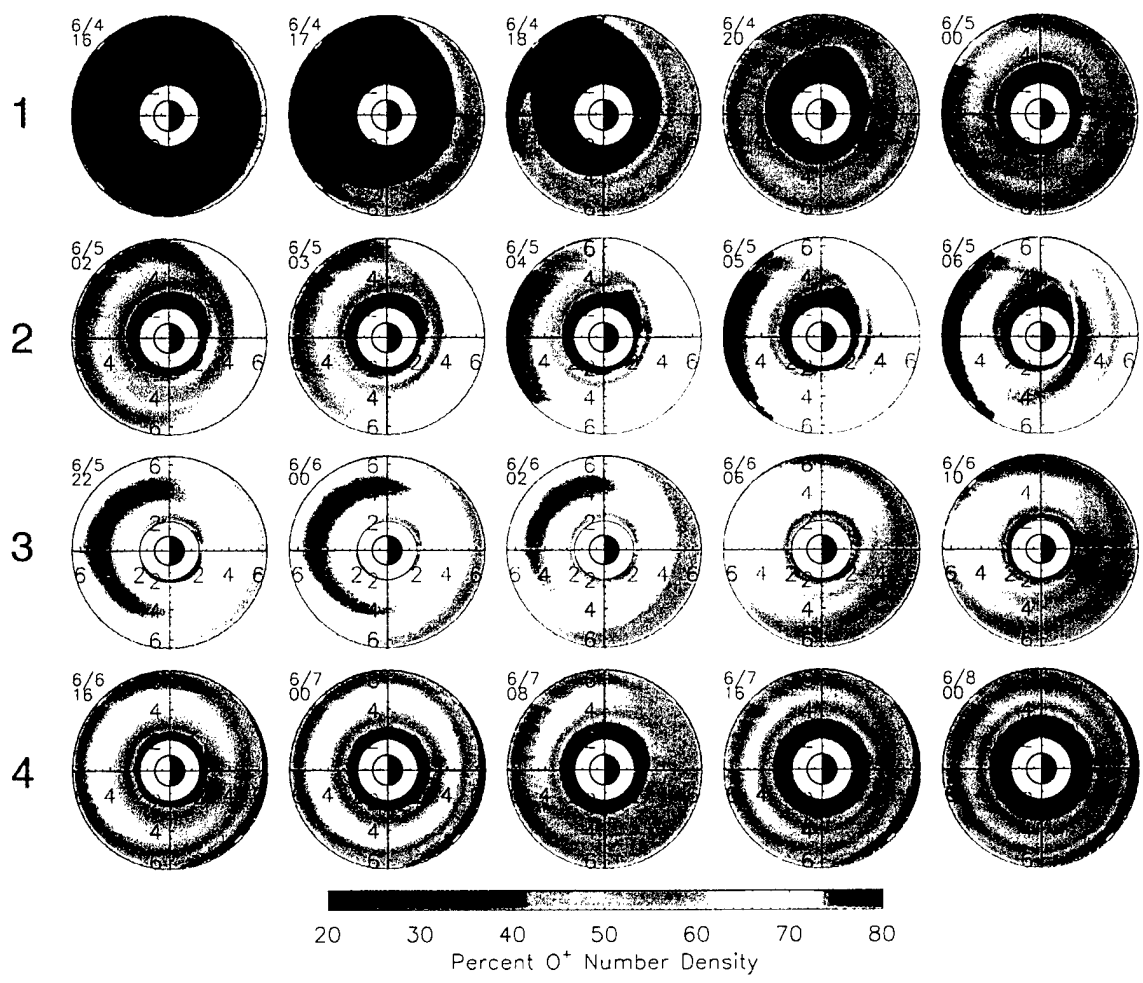
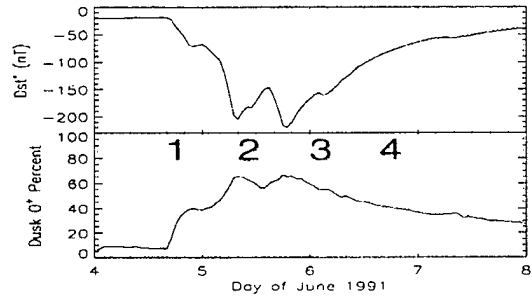


Plate 4. Dial plots of O<sup>+</sup> percentage of number density showing oxygen-rich plasma sweeping through the system during the main phase development and oxygen-poor plasma replacing it as the activity level declines during the recovery phase. Also shown is modeled Dst\* and globally averaged O<sup>+</sup> percent contribution to that value.

charge-exchange collisions because it is trapped on closed drift paths with no access to the dayside magnetopause. This is indicated by the darkening and gradual thickening of the inner ring of charge exchange loss, which maximizes at the deepest radial penetration of the ring current and moves outward with time. During this interval, composition changes occur slowly.

Further evidence for  $O^+$  dominance during the main phase but not in the recovery phase for this storm was given by *Liemohn et al.* [2000]. In that study, heating rates from the ring current ions to the thermal electrons were calculated from model results. A large  $O^+$  content was needed to achieve the heating rates to the thermal electrons necessary to match observed temperatures at Millstone Hill during the main phase and early recovery of the storm. Later in the storm, however, the temperatures dropped considerably, and a corresponding drop in  $O^+$  content was needed to match the observations. This strong  $O^+$  dependence of the energy deposition rates occurs because the thermal electrons most efficiently interact with ring current ions of a few keV for  $H^+$  and a few tens of keV for  $O^+$  [cf. *Kozyra et al.*, 1987]. Because the peak of the ring current energy spectra occurs near 50 keV, the hot oxygen ions in the inner magnetosphere are responsible for most of the ring current energy input into the thermal electrons.

Note that the *Young et al.* [1982] relation cannot, because of its statistical nature, account for the actual variation during a particular event. Rather, timing of the ionospheric loading and unloading of the tail with respect to the storm phases is responsible for this changeover. This difference could account for the differences between the modeled and observed composition (Figures 5 and 7). Regardless of what the process is that brings the ionospheric material into the lobes and plasma sheet, it has been observed there by numerous studies [e.g., *Sharp et al.*, 1981; *Candidi et al.*, 1982; *Orsini et al.*, 1990; *Mukai et al.*, 1994; *Hirahara et al.*, 1996; *Seki et al.*, 1996; *Ashour-Abdalla et al.*, 1997], and quantified by the *Young et al.* [1982] relationship. However, the *Young et al.* [1982] formulas are based on data from an instrument that only measured up to 17 keV/e. While this captures a significant portion of the ion distribution function at geosynchronous orbit (compare with Figure 4c), it does not include the high-energy

tail of the distribution that was measured by the CRRES MICS instrument. While a statistical study of CRRES and Polar hot ion composition has been conducted [Roeder *et al.*, 2000], the results of that analysis have not yet been incorporated into the model. In the present study, this high energy tail (energy > 50 keV) has an O<sup>+</sup> content, which is assumed to be exponentially decreasing with energy. Inaccuracies introduced by this assumption could be a reason for the discrepancy between the RAM results and the observations, particularly at high energies and large L values. Figure 7c clearly shows that this assumption is good during quiet times, but underestimates the composition changes during the active period. The theory-data comparisons shown in Figures 7b and 7c imply that the composition of the ring current is largely controlled by the composition of the near-Earth plasma sheet. Conversely, an overestimate of the O<sup>+</sup> content in the high-energy range could also produce an overestimate of the ring current energy content by the RAM model (and thus Dst\*).

## 7.0 Summary and Conclusions

A simulation of the 4-6 June 1991 magnetic storm was undertaken to investigate the physical processes underlying the multi-stage Dst development, multi-stage decay and rapid mass-dependent early recovery phase losses. It was found that all 3 of these features were rooted in the fact that the main phase ring current is a partial ring current. Ring current ions make only one pass through the inner magnetosphere as they drift along open drift paths that intersect the dayside magnetopause. This means that changes in the inner plasmasheet source population are directly transmitted along these open drift paths to affect the characteristics of the stormtime ring current. The “flow-out” of ring current ions at the dayside magnetopause, in the presence of a decreasing plasma sheet source density and weakening convection electric field, accounts for the fast decay time scales in storms exhibiting a two-phase decay. Weakening of the convection electric field drives the conversion of open to closed drift paths during the early recovery phase, trapping ring current plasma on closed drift paths and producing a symmetric ring current by the beginning of the late recovery phase. This trapped plasma decays more slowly, mostly through

charge exchange collisions with the hydrogen geocorona. The change from rapid "flow-out" time scales to slower "charge-exchange" time-scales is responsible for the pronounced two-phase decay typically seen during the recovery of large storms. The June 1991 storm actually exhibits a 3-phase decay: an initial phase where charge-exchange dominates the loss followed by a characteristic 2-phase decay

The main results of the present study are as follows:

- (1) The dramatic composition changes, that occur in the ring current during the early recovery phase of the 4-6 June 1991 storm which ended around 12 UT on June 5, result mainly from the changes in composition of the plasma sheet as the magnetic activity decreases. There is a temporary additional loss of  $O^+$  through charge-exchange collisions during a northward IMF interval at the start of the recovery phase but as soon as the IMF turned southward again the ring current quickly took on the composition of the plasma sheet source. As the early recovery phase continues in the presence of decreasing magnetic activity, increasingly oxygen-poor plasma sheet source populations sweep through the inner magnetosphere on open drift paths which are gradually being converted to closed drift paths. At the same time, the more oxygen-rich populations, associated with the main phase plasma sheet source, are being lost at the dayside magnetopause. This transition from relatively oxygen-rich to oxygen-poor plasma occurs throughout the early recovery phase. The populations that are eventually trapped to form the symmetric ring current are relatively oxygen-poor compared to the main phase ring current and decay slowly mostly through charge exchange collisions with the hydrogen geocorona.
- (2) A two-phase decay, defined as an abrupt change in the  $Dst^*$  recovery rate, is coincident with a switch from flow-out to charge exchange dominance of ring current energy loss. Charge exchange alone can cause such an abrupt transition only if the ring current is decaying perfectly at two very distinct time scales. Such a

situation is true for a two-species (e.g., H<sup>+</sup> and O<sup>+</sup>) ring current, but only if it is sharply peaked in energy, pitch angle, and L shell. This scenario has never been observed. In general, the ring current ions span a broad range in energy, pitch angle, and L shell, and the charge exchange decay rate is given by the superposition of many loss lifetimes. This plethora of ring current loss time-scales explains the findings of *Campbell* [1996] that the stormtime Dst profile resembles a lognormal distribution (a curve created by the superposition of many growth and decay rates). The net result of a purely charge-exchange decay is a gradual shift toward longer time-scales as the storm recovery progresses (see the dotted curve in Figure 7e). An abrupt change in the decay rate requires an abrupt transition between mechanisms causing the decay, as is the case when "flow-out" ceases.

- (3) The *Young et al.* [1982] composition formulas, which are based on observations of ions with energy  $\leq 17$  keV/e in the near-Earth plasma sheet, work quite well at reproducing the observed overall ring current composition. This is because the plasma sheet ions with energy below 20 keV are adiabatically energized to form the bulk of the storm-time ring current at lower L values.
- (4) "Flow-out" losses were amplified during intervals of high solar wind dynamic pressure in which the magnetopause was eroded inside of geosynchronous orbit. This process may reduce the strength of a ring current produced in the presence of high solar wind dynamic pressure.
- (5) Plasma sheet density variations have an important role in multi-stage ring current developments. The main phase of the June 1991 storm was complicated, consisting of three separate ring current intensifications. Simulation results for this storm indicate that preceding intensifications (pre-existing ring currents) did not act as preconditioning elements for later intensifications but instead were swept out of the magnetosphere on open drift paths by later bursts of strong convection. Enhancements in the inner plasma sheet density were responsible for the second

intensification being of comparable magnitude to the third despite the fact that convection electric fields were weaker. It is suggested that preconditioning occurs in a multi-step magnetic storm development through the cumulative effects of the sequence of solar wind drivers on the plasma populations that form the near-Earth plasma sheet [c.f., *Kozyra et al.*, 1998a].

These results demonstrate the far-reaching consequences of having a main-phase ring current that is largely on open drift-paths, consequences for two-stage Dst development [*Kamide et al.*, 1998] and for composition changes, which typically mirror Dst variations during all stages of the storm [c.f., *Daglis*, 1997]. Moreover, they also demonstrate the influence of plasma sheet dynamics on ring current dynamics, lending further urgency to the questions of what produces plasma sheet density, temperature and composition changes during magnetic storms and how these changes are related to upstream solar wind conditions.

**Acknowledgments.** This work was supported by NASA grant NAG5-4771 and NSF contracts ATM-9711381 and ATM-9800830. The authors would like to thank T. W. Garner for useful discussions regarding this topic and also for access to his dissertation. The MBI was provided by the USAF Research Laboratory, Hanscom AFB, MA, and the authors would like to thank S. Gussenhoven for useful discussions regarding this index and magnetospheric convection. The solar wind and IMF data are from the CDAWeb ISTP Key Parameter database, and the Kp and Dst indices are from the Kyoto World Data Center-C2 in Kyoto, Japan.

## References

- Ashour-Abdalla, M., et al., Ion sources and acceleration mechanisms inferred from local distribution functions, *Geophys. Res. Lett.*, 24, 955, 1997.
- Belian, R. D., G. R. Gisler, T. Cayton, and R. Christensen, High-Z energetic particles at geosynchronous orbit during the great solar proton event series of October 1989, *J. Geophys. Res.*, 97, 16,897, 1992.
- Bourdarie, W., D. Boscher, T. Beutier, J.-A. Sauvaud, and M. Blanc, Electron and proton radiation belt dynamic simulations during storm periods: A new asymmetric convection-diffusion model, *J. Geophys. Res.*, 102, 17,541, 1997.
- Burke, W. J., N. C. Maynard, M. P. Hagan, R. A. Wolf, G. R. Wilson, L. C. Gentile, M. S. Gussenhoven, C. Y. Huang, T. W. Garner, and F. J. Rich, Electrodynamics of the inner magnetosphere observed in the dusk sector by CRRES and DMSP during the magnetic storm of June 4 - 6, 1991, *J. Geophys. Res.*, 103, 29,399-29,418, 1998.
- Burton, R. K., R. L. McPherron, and C. T. Russell, An empirical relationship between interplanetary conditions and Dst, *J. Geophys. Res.*, 80, 4204-4214, 1975.
- Candidi, M., S. Orsini, and V. Formisano, The properties of ionospheric O<sup>+</sup> ions as observed in the magnetotail boundary layer and northern plasma lobe, *J. Geophys. Res.*, 87, 9097, 1982.
- Carovillano, R. L., and G. L. Siscoe, Energy and momentum theorems in magnetospheric processes, *Rev. of Geophys. Space Phys.*, 11, 289-353, 1973
- Chen, M. W., L. R. Lyons, and M. Schulz, Simulations of phase space distributions of storm time proton ring current, *J. Geophys. Res.*, 99, 5745, 1994.
- Chen, M. W., J. L. Roeder, J. F. Fennell, L. R. Lyons, and M. Schulz, Simulations of ring current proton pitch angle distributions, *J. Geophys. Res.*, 103, 165, 1998.
- Chen, M. W., J. L. Roeder, J. F. Fennell, L. R. Lyons, R. L. Lambour, and M. Schulz, Proton ring current pitch angle distributions: Comparison of simulations with CRRES observations, *J. Geophys. Res.*, 104, 17,379, 1999.

- Chen, M. W., L. R. Lyons, and M. Schulz, Stormtime ring-current formation: A comparison between single- and double-dip model storms with similar transport characteristics, *J. Geophys. Res.*, *106*, 27,755, 2000.
- Daglis, I. A., The role of magnetosphere-ionosphere coupling in magnetic storm dynamics, in *Magnetic Storms*, Geophysical Monograph Series, vol. 98, Tsurutani, B. T., Gonzalez, W. D., Kamide, Y., Arballo, J. K. (Eds.), p. 107-116, American Geophysical Union, 1997.
- Daglis, I.A., R. M. Thorne, W. Baumjohann, S. Orsini, The terrestrial ring current: origin, formation and decay, *Rev. Geophys.*, *37*, 407-38, 1999.
- Dessler, A. J., and E. N. Parker, Hydromagnetic theory of geomagnetic storms, *J. Geophys. Res.*, *64*, 2239-2252, 1959.
- Ebihara, Y., and M. Ejiri, Modeling of solar wind control of the ring current buildup: A case study of the magnetic storms in April 1997, *Geophys. Res. Lett.*, *25*, 3751, 1998.
- Ebihara, Y., and M. Ejiri, Simulation study on fundamental properties of the storm-time ring current, *J. Geophys. Res.*, *105*, 15,843, 2000.
- Elphic, R. C., L. A. Weiss, M. F. Thomsen, D. J. McComas, and M. B. Moldwin, Evolution of plasmaspheric ions at geosynchronous orbit during times of high geomagnetic activity, *Geophys. Res. Lett.*, *23*, 2189, 1996.
- Fok, M.-C., J. U. Kozyra, A. F. Nagy and T. E. Cravens, Lifetime of ring current particles due to Coulomb collisions in the plasmasphere, *J. Geophys. Res.*, *96*, 7861-7867, 1991.
- Fok, M.-C., J. U. Kozyra, A. F. Nagy, C. E. Rasmussen, and G. V. Khazanov, A decay model of equatorial ring current and the associated aeronomical consequences, *J. Geophys. Res.*, *98*, 19,381, 1993.
- Fok, M.-C., T. E. Moore, J. U. Kozyra, G. C. Ho, and D. C. Hamilton, Three-dimensional ring current decay model, *J. Geophys. Res.*, *100*, 9619, 1995.
- Fok, M.-C., T. E. Moore, and M. E. Greenspan, Ring current development during storm main phase, *J. Geophys. Res.*, *101*, 15,311, 1996.

- Garner, T. W., A case study of the June 4-5, 1991 magnetic storm using the Rice Convection Model, Doctoral Thesis, Rice University, Houston, Texas, 2000.
- Gloeckler, G. and D. C. Hamilton, AMPTE ion composition results, *Phys. Scripta*, T18, 73, 1987.
- Gonzalez, W. D., and B. T. Tsurutani, Criteria of interplanetary parameters causing intense magnetic storms ( $Dst < -100$  nT), *Planet. Space Sci.*, 35, 1101, 1987.
- Gonzalez, W. D., B. T. Tsurutani, A. L. C. Gonzalez, E. J. Smith, F. Tang, and S.-I. Akasofu, Solar wind-magnetosphere coupling during intense magnetic storms (1978-1979), *J. Geophys. Res.*, 94, 8835, 1989.
- Gonzalez, W. D., J. A. Joselyn, Y. Kamide, H. W. Kroehl, G. Rostoker, B. T. Tsurutani and V. M. Vasyliunas, What is a geomagnetic storm?, *J. Geophys. Res.*, 99, 5771-92, 1994.
- Gonzalez, W. D., B. T. Tsurutani, A. L. Clua De Gonzalez, Interplanetary origin of geomagnetic storms, *Space Sci. Rev.*, 88, 529-562, 1999.
- Gussenhoven, M. S., D. A. Hardy, and N. Heinemann, Systematics of the equatorward diffuse auroral boundary, *J. Geophys. Res.*, 88, 5692, 1983.
- Hamilton, D. C., G. Gloeckler, F. M. Ipavich, W. Studemann, B. Wilkey, and G. Kremser, Ring current development during the great geomagnetic storm of February 1986, *JGR*, 93, 14343, 1988.
- Harel, M., R. A. Wolf, P. H. Reiff, R. W. Spiro, W. J. Burke, F. J. Rich, and M. Smiddy, Quantitative simulation of a magnetospheric substorm 1. Model logic and overview, *J. Geophys. Res.*, 86, 2217, 1981.
- Hirahara, M., T. Mukai, T. Terasawa, S. Machida, Y. Saito, T. Yamamoto, and S. Kokubun, Cold dense ion flows with multiple components observed in the distant tail lobe by Geotail, *J. Geophys. Res.*, 101, 7769, 1996.
- Jaggi, R. K., and R. A. Wolf, Self-consistent calculation of the motion of a sheet of ions in the magnetosphere, *J. Geophys. Res.*, 78, 2842, 1973.

- Jordanova, V. K., J. U. Kozyra, G. V. Khazanov, A. F. Nagy, C. E. Rasmussen, and M.-C. Fok, A bounce-averaged kinetic model of the ring current ion population, *Geophys. Res. Lett.*, *21*, 2785, 1994.
- Jordanova, V. K., L. M. Kistler, J. U. Kozyra, G. V. Khazanov, and A. F. Nagy, Collisional losses of ring current ions, *J. Geophys. Res.*, *101*, 111-126, 1996.
- Jordanova, V. K., J. U. Kozyra, A. F. Nagy, and G. V. Khazanov, Kinetic model of the ring current-atmosphere interactions, *J. Geophys. Res.*, *102*, 14,279, 1997.
- Jordanova, V. K., C. J. Farrugia, L. Janoo, J. M. Quinn, R. B. Torbert, K. W. Ogilvie, R. P. Lepping, J. T. Steinberg, D. J. McComas, and R. D. Belian, October 1995 magnetic cloud and accompanying storm activity: Ring current evolution, *J. Geophys. Res.*, *103*, 79, 1998.
- Jordanova, V. K., R. B. Torbert, R. M. Thorne, H. L. Collin, J. L. Roeder, and J. C. Foster, Ring current activity during the early  $B_z < 0$  phase of the January 1997 magnetic cloud, *J. Geophys. Res.*, *104*, 24,895-24,914, 1999.
- Kamide, Y., N. Yokoyama, W. Gonzalez, B. T. Tsurutani, I. A. Daglis, A. Brekke, and S. Masuda, Two-step development of geomagnetic storms, *J. Geophys. Res.*, *103*, 6917-21, 1998.
- Koga, R., S. S. Imamoto, N. Katz, and S. D. Pinkerton, Data processing units for eight magnetospheric particle and field sensors, *J. Spacecraft and Rockets*, *29*, 574, 1992.
- Kozyra, J. U., E. G. Shelley, R. H. Comfort, L. H. Brace, T. E. Cravens, and A. F. Nagy, The role of ring current  $O^+$  in the formation of stable auroral red arcs, *J. Geophys. Res.*, *92*, 7487-7502, 1987.
- Kozyra, J. U., J. E. Borovsky, M. W. Chen, M.-C. Fok, and V. K. Jordanova, Plasma sheet preconditioning, enhanced convection and ring current development, in *Substorms-4*, Edited by S. Kokubun, and Y. Kamide, by Terra Scientific Publishing Co./Kluwer Academic Publishers, 755, 1998a.

- Kozyra, J.U., M.C. Fok, E. R. Sanchez, D. S. Evans, D. C. Hamilton and A. F. Nagy, The role of precipitation losses in producing the rapid early recovery phase of the great magnetic storm of February 1986, *J. Geophys. Res.*, *103*, 6801, 1998b.
- Kozyra, J. U., V. K. Jordanova, J. E. Borovsky, M. F. Thomsen, D. J. Knipp, D. S. Evans, D. J. McComas, and T. E. Cayton, Effects of a high-density plasma sheet on ring current development during the November 2-6, 1993, magnetic storm, *J. Geophys. Res.*, *103*, 26,285-26,305, 1998c.
- Lambour, R. L., L. A. Weiss, R. C. Elphic, and M. F. Thomsen, Global modeling of the plasmasphere following storm sudden commencements, *J. Geophys. Res.*, *102*, 24,351, 1997.
- Langel, R. A., and R. H. Estes, Large-scale, near-field magnetic fields from external sources and the corresponding induced magnetic field, *J. Geophys. Res.*, *90*, 2487, 1985.
- Liemohn, M. W., J. U. Kozyra, V. K. Jordanova, G. V. Khazanov, M. F. Thomsen, and T. E. Cayton, Analysis of early phase ring current recovery mechanisms during geomagnetic storms, *Geophys. Res. Lett.*, *26*, 2845-2849, 1999.
- Liemohn, M. W., J. U. Kozyra, P. G. Richards, G. V. Khazanov, M. J. Buonsanto, and V. K. Jordanova, Ring current heating of the thermal electrons at solar maximum, *J. Geophys. Res.*, *106*, 27,767, 2000.
- Liemohn, M. W., J. U. Kozyra, M. F. Thomsen, J. L. Roeder, G. Lu, J. E. Borovsky, and T. E. Cayton, The dominant role of the asymmetric ring current in producing the stormtime Dst\*, *J. Geophys. Res.*, *106*, 10,883, 2001a.
- Liemohn, M. W., J. U. Kozyra, C. R. Clauer, and A. J. Ridley, Computational analysis of the near-Earth magnetospheric current system during two-phase decay storms, *J. Geophys. Res.*, *106*, in press, 2001b.
- Lui, A. T. Y., and D. C. Hamilton, Radial profiles of quiet time magnetospheric parameters, *J. Geophys. Res.*, *97*, 19,325, 2000.
- Lyons, L. R., and D. J. Williams, *Quantitative Aspects of Magnetospheric Physics*, D. Reidel Publ. Co., Dordrecht-Holland, 1984

- Lyons, L. R., and M. Shulz, Acces of energetic particles to storm time ring current through enhanced radial "diffusion", *J. Geophys. Res.*, 94, 5491-5496, 1989.
- Mauk, B. H., and C. E. McIlwain, Correlation of Kp with the substorm-injected plasma boundary, *J. Geophys. Res.*, 79, 3193, 1974.
- Mayaud, P. N., *Derivation, Meaning, and Use of Geomagnetic Indices, Geophys. Monogr. Ser.*, vol. 22, AGU, Washington, DC, 1980.
- McComas, D. J., S. J. Bame, B. L. Barraclough, J. R. Donart, R. C. Elphic, J. T. Gosling, M. B. Moldwin, K. R. Moore, and M. F. Thomsen, Magnetospheric plasma analyzer: initial three-spacecraft observations from geosynchronous orbit, *J. Geophys. Res.*, 98, 13,453, 1993.
- McIlwain, C. E., A Kp-dependent equatorial electric field model, *Adv. Space Res.*, 6(3), 187, 1986.
- Moldwin, M. B., M. I. Fernandez, H. K. Rassoul, M. F. Thomsen, S. J. Bame, D. J. McComas, and J. F. Fennell, A reexamination of the local time asymmetry of lobe encounters at geosynchronous orbit: CRRES, ATS 5, and LANL observations, *J. Geophys. Res.*, 103, 9207, 1998.
- Mukai, T., M. Hirahara, S. Machida, Y. Saito, T. Terasawa, and A. Nishida, Geotail observation of cold ion streams in the medium distance magnetotail lobe in the course of a substorm, *Geophys. Res. Lett.*, 21, 1023, 1994.
- O'Brien, T. P., and R. L. McPherron, An empirical phase space analysis of ring current dynamics: Solar wind control of injection and decay, *J. Geophys. Res.*, 105, 7707, 2000.
- Orsini, S., M. Candidi, M. Stokholm, and H. Balsiger, Injection of ionospheric ions into the plasma sheet, *J. Geophys. Res.*, 95, 7915, 1990.
- Richmond, A. D., and Y. Kamide, Mapping electrodynamic features of the high-latitude ionosphere from localized observations: Technique, *J. Geophys. Res.*, 93, 5741, 1988.
- Roeder, J. L., J. F. Fennell, M. W. Chen, M. Schulz, M. Gande, and S. Livi, CRRES observations of the composition of the ring-current ion populations, *Adv. Space Res.*, 17(10), 17-24, 1996a.

- Roeder, J. L., J. F. Fennell, M. W. Chen, M. Grande, S. Livi, and M. Schulz, CRRES observations of stormtime ring current ion composition, in *Workshop on the Earth's trapped particle environment*, AIP Conference Proceedings, vol. 383, Reeves, G. D. (Ed.), p. 131-143, American Institute of Physics, 1996b.
- Roeder, J. L., J. F. Fennell, M. Grande, and S. Livi, Solar cycle effects on stormtime ring current ion composition: CRRES and Polar observations, *Eos Trans. AGU*, 81(48), Fall Meet. Suppl., F1045, 2000.
- Scokopke, N., A general relation between the energy of trapped particles and the disturbance field near the earth, *J. Geophys. Res.*, 71, 3125-3130, 1966.
- Seki, K., M. Hirahara, T. Terasawa, I. Shinohara, T. Mukai, Y. Saito, S. Machida, T. Yamamoto, and S. Kokubun, Coexistence of Earth-origin O<sup>+</sup> and solar wind-origin H<sup>+</sup>/He<sup>++</sup> in the distant magnetotail, *Geophys. Res. Lett.*, 23, 985, 1996.
- Senior, C., D. Fontaine, G. Caudal, D. Alcaydé, and J. Fontanari, Convection electric fields and electrostatic potential over 61° <  $\Lambda$  < 72° invariant latitude observed with the European incoherent scatter facility, 2, Statistical results, *Ann. Geophys.*, 8, 257-272, 1989.
- Sharp, R. D., D. L. Carr, W. K. Peterson, and E. G. Shelley, Ion streams in the magnetotail, *J. Geophys. Res.*, 86, 4639, 1981.
- Shue, J.-H., P. Song, C. T. Russell, J. T. Steinberg, J. K. Chao, G. Zastenker, O. L. Vaisberg, S. Kokubun, H. J. Singer, T. R. Detman, and H. Kawano, Magnetopause location under extreme solar wind conditions, *J. Geophys. Res.*, 103, 17,691-17,700, 1998.
- Spiro, R. W., and R. A. Wolf, Electrodynamics of convection in the inner magnetosphere, in *Magnetospheric Currents*, AGU Monogr. Ser., vol. 28, edited by T. A. Potemra, p. 247, AGU, Washington, D. C., 1984.
- Takahashi, S., T. Iyemori, and M. Takeda, A simulation of the storm-time ring current, *Planet. Space Sci.*, 38, 1133, 1990.
- Takahashi, S., M. Takeda, and Y. Yamada, Simulation of storm-time partial ring current system and the dawn-dusk asymmetry of geomagnetic variation, *Planet. Space Sci.*, 39, 821, 1991.

- Thomsen, M. F., J. E. Borovsky, D. J. McComas, and M. R. Collier, Variability of the ring current source population, *Geophys. Res. Lett.*, 25, 3481-4, 1998.
- Thomsen, M. F., E. Noveroske, J. E. Borovsky, and D. J. McComas, Calculation of moments from measurements by the Los Alamos Magnetospheric Plasma Analyzer, internal report LA-13566-MS, Los Alamos National Laboratory, New Mexico, May 1999.
- Tsurutani, B. T., W. D. Gonzalez, F. Tang, Y. T. Lee, and M. Okada, Reply to L. J. Lanzerotti: Solar wind ram pressure corrections and an estimation of the efficiency of viscous interaction, *Geophys. Res. Lett.*, 19, 1993, 1992.
- Tsyganenko, N., Modeling the inner magnetosphere: The asymmetric ring current and Region 2 Birkeland currents revisited, *J. Geophys. Res.*, 105, 27,739-27,754, 2000.
- Weiss, L. A., R. L. Lambour, R.C. Elphic, and M. F. Thomsen, Study of plasmaspheric evolution using geosynchronous observations and global modeling, *Geophys. Res. Lett.*, 24, 599, 1997.
- Wilken B., W. Weiss, D. Hall, M. Grande, F. Soraas, and J. F. Fennel, Magnetospheric ion composition spectrometer onboard the CRRES spacecraft, *J. Spacecraft and Rockets*, 29, 595, 1992.
- Wodnicka, E. B., The magnetic storm main phase modeling, *Planet. Space Sci.*, 37, 525, 1989.
- Wodnicka, E. B., What does the magnetic storm development depend on?, *Planet. Space Sci.*, 39, 1163, 1991.
- Wolf, R. A., The quasi-static (slow-flow) region of the magnetosphere, in *Solar-Terrestrial Physics: Principles and Theoretical Foundations*, edited by R. L. Carovillano and J. M. Forbes, p. 303, D. Reidel, Norwell, Mass., 1983.
- Wolf, R. A., and R. W. Spiro, Numerical modeling of the ring current and plasmasphere, *Space Sci. Rev.*, 80, 199, 1997.
- Wolf, R. A., M. Harel, R. W. Spiro, G.-H. Voigt, P. H. Reiff, and C. K. Chen, Computer simulation of inner magnetospheric dynamics for the magnetic storm of July 29, 1977, *J. Geophys. Res.*, 87, 5949, 1982.

Wolf, R. A., J. W. Freeman, Jr., B. A. Hausman, R. W. Spiro, R. V. Hilmer, and R. L. Lambour, Modeling convection effects in magnetic storms, in *Geomagnetic Storms, AGU Monogr. Ser.*, vol. 98, edited by B. T. Tsurutani, J. K. Arballo, W. D. Gonzalez, and Y. Kamide, p. 161, AGU, Washington, D. C., 1997.

Young, D. T., H. Balsiger, and J. Geiss, Correlations of magnetospheric ion composition with geomagnetic and solar activity, *J. Geophys. Res.*, 87, 9077-9096, 1982.

## LABORATORY OPERATIONS

The Aerospace Corporation functions as an "architect-engineer" for national security programs, specializing in advanced military space systems. The Corporation's Laboratory Operations supports the effective and timely development and operation of national security systems through scientific research and the application of advanced technology. Vital to the success of the Corporation is the technical staff's wide-ranging expertise and its ability to stay abreast of new technological developments and program support issues associated with rapidly evolving space systems. Contributing capabilities are provided by these individual organizations:

**Electronics and Photonics Laboratory:** Microelectronics, VLSI reliability, failure analysis, solid-state device physics, compound semiconductors, radiation effects, infrared and CCD detector devices, data storage and display technologies; lasers and electro-optics, solid state laser design, micro-optics, optical communications, and fiber optic sensors; atomic frequency standards, applied laser spectroscopy, laser chemistry, atmospheric propagation and beam control, LIDAR/LADAR remote sensing; solar cell and array testing and evaluation, battery electrochemistry, battery testing and evaluation.

**Space Materials Laboratory:** Evaluation and characterizations of new materials and processing techniques: metals, alloys, ceramics, polymers, thin films, and composites; development of advanced deposition processes; nondestructive evaluation, component failure analysis and reliability; structural mechanics, fracture mechanics, and stress corrosion; analysis and evaluation of materials at cryogenic and elevated temperatures; launch vehicle fluid mechanics, heat transfer and flight dynamics; aerothermodynamics; chemical and electric propulsion; environmental chemistry; combustion processes; space environment effects on materials, hardening and vulnerability assessment; contamination, thermal and structural control; lubrication and surface phenomena.

**Space Science Applications Laboratory:** Magnetospheric, auroral and cosmic ray physics, wave-particle interactions, magnetospheric plasma waves; atmospheric and ionospheric physics, density and composition of the upper atmosphere, remote sensing using atmospheric radiation; solar physics, infrared astronomy, infrared signature analysis; infrared surveillance, imaging, remote sensing, and hyperspectral imaging; effects of solar activity, magnetic storms and nuclear explosions on the Earth's atmosphere, ionosphere and magnetosphere; effects of electromagnetic and particulate radiations on space systems; space instrumentation, design fabrication and test; environmental chemistry, trace detection; atmospheric chemical reactions, atmospheric optics, light scattering, state-specific chemical reactions and radiative signatures of missile plumes.

**Center for Microtechnology:** Microelectromechanical systems (MEMS) for space applications; assessment of microtechnology space applications; laser micromachining; laser-surface physical and chemical interactions; micropropulsion; micro- and nanosatellite mission analysis; intelligent microinstruments for monitoring space and launch system environments.

**Office of Spectral Applications:** Multispectral and hyperspectral sensor development; data analysis and algorithm development; applications of multispectral and hyperspectral imagery to defense, civil space, commercial, and environmental missions.



2350 E. El Segundo Boulevard  
El Segundo, California 90245-4691  
U.S.A.